Chapter 5

Ocean Models

5.1 Summary

(i) JMA operates two high-resolution MGDSST and HIMSST analyses based on satellite remote sensing data and *in-situ* observation data to provide real-time information on sea surface temperature. The former covers the global area with a horizontal resolution of 0.25°, and the latter covers the western North Pacific with a higher resolution of 0.1°. The Agency also conducts global analysis with a resolution of 1° based only on *in-situ* observation data (COBE-SST2) for consistent monitoring of long-term ocean variations in phenomena such as El Niño events and global warming.

(ii) JMA has operated cascading ocean data assimilation systems since 2008 based on a unified ocean data assimilation framework known as the Multivariate Ocean Variational Estimation/Meteorological Research Institute Community Ocean Model (MOVE/MRI.COM) developed by the Agency's Meteorological Research Institute (MRI). Two such systems (MOVE-G3 and MOVE-JPN) are currently in operation. MOVE-G3 analyzes the global ocean to monitor El Niño and initializes the oceanic part of the coupled seasonal prediction system. MOVE-JPN is used for the analysis and prediction of oceanographic sub-mesoscale events and sea ice conditions over coastal areas around Japan.

(iii) JMA operates the Global Wave Model (GWM), the Coastal Wave Model (CWM) and the Wave Ensemble System (WENS) as ocean wave models. All three are based on the MRI-III, the third-generation wave model developed by MRI. The WENS was developed to provide probabilistic information on ocean waves in medium-range forecasts. The Shallow-water Wave Model (SWM) is also operated in trial mode to predict ocean waves in bays and nearshore areas around Japan with a higher horizontal resolution of 1 arc minute.

(iv) JMA operates the Japan Area storm surge model, the Japan area storm surge probabilistic forecast system and the Asia area storm surge ensemble prediction system. The Japan area storm surge model covers the Japan region and predicts storm surges generated by tropical and extra-tropical cyclones for the Japanese coast. JMA began operating the Japan area storm surge probabilistic forecast system based on the Japan area storm surge model in 2022. The Asia area storm surge ensemble prediction system is for the Asian region and is developed within the WMO Storm Surge Watch Scheme framework. The system was updated from the Asia area storm surge model using the GSM and all members of GEPS in 2022. Horizontal storm surge maps and time-series charts for selected points are issued to Typhoon Committee Members.

(v) JMA's oil spill prediction model was introduced in 1999. Operation is triggered when a large-scale oil spill occurs offshore. The effects of transport by sea surface winds, ocean waves and sea surface currents, turbulent diffusion, evaporation, and emulsification are considered.

5.2 Sea Surface Temperature Analysis

5.2.1 Merged Satellite and *In-situ* Data Global Daily Sea Surface Temperature (MGDSST)

Daily sea surface temperatures (SSTs) in the global ocean on a grid of $0.25 \times 0.25°$ are objectively analyzed to support ocean information services (Kurihara *et al.* 2006). The data are also used as boundary conditions for atmospheric short- and medium-range prediction models (see Section 3.2 and Section 3.3) and as observational data in the ocean data assimilation system (see Section 5.3). SST data obtained from satellite infrared sensors (Suomi-NPP/VIIRS, NOAA-20/VIIRS) and microwave sensors (GCOM-W/AMSR2) are used together with *in-situ* SST observations. Many *in-situ* data are obtained through the Global Telecommunication System, but domestic organizations also provide large amounts of data by e-mail.

Satellite-derived SST anomalies (SSTAs) from daily SST climatologies are decomposed into large/medium/small scales with cutoff wavelengths of 580, 143 and 55km, respectively, and into long- and short-time scales with cutoff periods of 53 and 10 days, respectively. The medium scale is intended to represent SST signals caused by mesoscale (eddy-scale) phenomena, and the small scale to represent front signals. Long-time scale signals represent intra-seasonal variations, and short-time scale signals represent variations influenced by atmospheric conditions such as tropical cyclones. Short-time signals are further processed by division into 27-53- and 10-27-day components, and only AMSR2 data are used for the latter. Signals varying with a period shorter than 10 days are cut off due to their significant data noise content.

The large scale and long-time scale components of SSTAs from satellites are calibrated with *in-situ* SSTAs using Poisson's equation (Reynolds 1987). Space-time optimum interpolation (OI) is applied to each component, and a zero value is adopted as the first guess. Space-time correlation coefficients and RMS values of the first guess error and satellite observation errors are statistically estimated a priori from satellite data using the method of Kuragano and Kamachi (2000). The daily SST is the sum of components of interpolated SSTAs and daily climatologies (Figure 5.2.1).
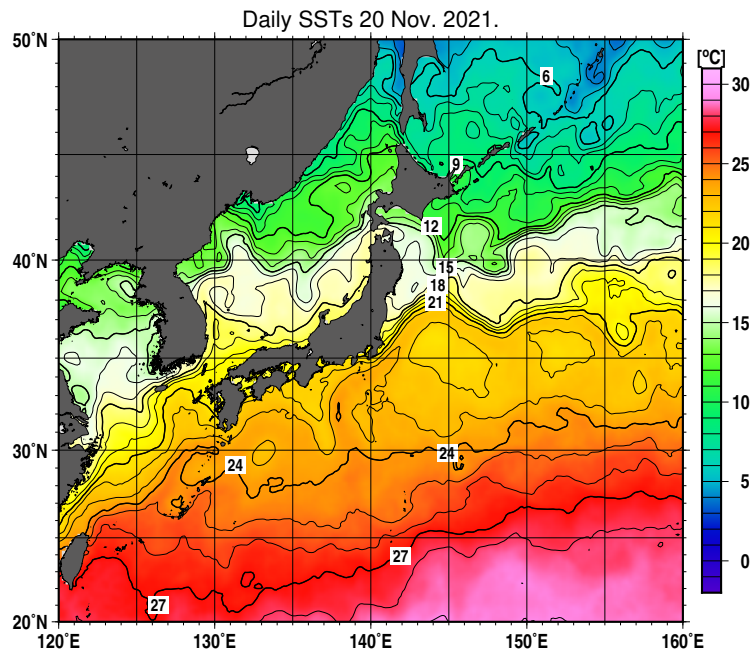

Figure 5.2.1: Sample SST analysis

5.2.2 HIgh-resolution Merged satellite and *In-situ* data Sea Surface Temperature (HIMSST)

SST analysis with high resolution is expected to provide optimal information variables such as boundary conditions for NWP models. Regional daily high-resolution ($0.1 \times 0.1°$) SST analysis for the western North Pacific (HIMSST) began in November 2016. In this work, the HIMSST analysis framework is based on that of MGDSST, in which satellite-derived SSTs are decomposed into several spatio-temporal components and analyzed via optimum interpolation (OI).

In addition to the satellite data used in MGDSST, JMA Himawari-9 L3 SSTs produced with a $0.02 \times 0.02°$ horizontal grid resolution and 10-minute intervals are incorporated into HIMSST analysis. JMA Himawari-9 L3 SSTs are calculated using a quasi-physical algorithm (Kurihara *et al.* 2016) and masked using JMA's cloud mask product (Imai and Yoshida 2016). More frequent geostationary meteorological satellite observation supports shorter time-scale components with periods from 10 days to 27 days in HIMSST analysis.

Suomi-NPP/VIIRS and NOAA-20/VIIRS SSTs and Himawari SSTs are converted into daily SST anomalies on a $0.1 \times 0.1°$ grid and decomposed into small scale with cut-off wavelengths from 22 to 143 km, which are shorter than 55-143 km of MGDSST. Figure 5.2.2 shows daily HIMSSTs (left) and MGDSSTs (right) in the seas around Hokkaido, Japan. The HIMSSTs show sharper SST gradients due to the higher grid resolution and application of the shorter wavelength components of satellite-derived SSTs including Himawari-8/9.

HIMSSTs support JMA's ocean information services for the western North Pacific, and have also been used since March 2019 to provide boundary conditions for short-range NWP models such as the Meso-Scale Model (MSM) and the Local Forecast Model (LFM) (Section 3.5, Section 3.7). The analysis data are available from the NEAR-GOOS Regional Real Time Database (https://www.data.jma.go.jp/goos/data/database.html).
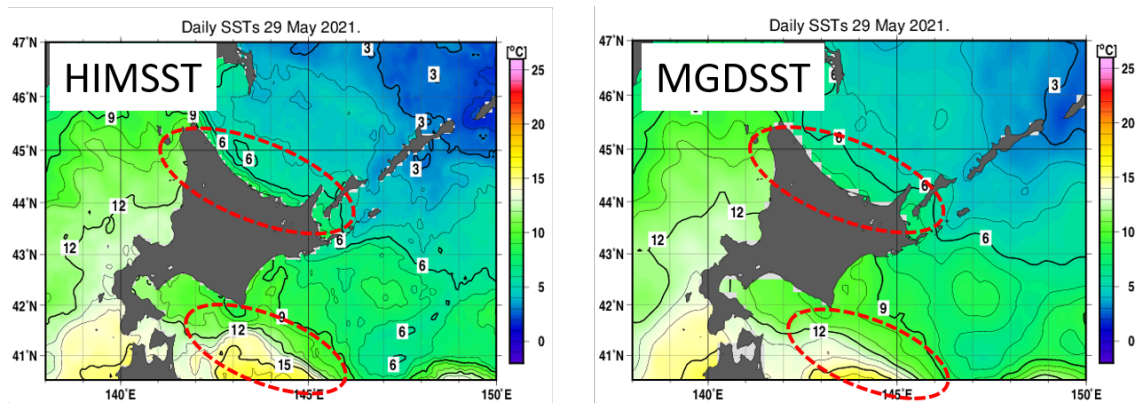

Figure 5.2.2: Comparison of HIMSST (left) and MGDSST (right) in the seas around Hokkaido.

5.2.3 Daily Sea Surface Analysis for Climate Monitoring

JMA terminated the production of its historical Sea Surface Temperature (SST) dataset with an analysis system called Centennial In Situ Observation-Based Estimates of the Variability of SST and Marine Meteorological Variables (COBE; Ishii *et al.* 2005) in March 2024. As a successor, COBE2 (Hirahara *et al.* 2014) began producing data in May 2021, and the COBE dataset was replaced with the COBE2 dataset in May 2023.

The SST component of COBE (COBE-SST) has a resolution of $1°$ latitude and $1°$ longitude. The east-west grid points start at $0.5°E$ and end at $0.5°W$, while the north-south points start at $89.5°S$ and end at $89.5°N$. Analysis is based on optimum interpolation, and the deviation of the previous day's analysis from the 1950-2000 normal is multiplied by 0.95 for use as a first guess. Information on sea ice concentration is used in the estimation of SSTs in polar oceans, and analysis is performed on a daily basis with data for seven days centered on the day of interest. Observations are aggregated daily for each call sign and averaged over a $1.5° \times 1.5°$ grid box to form super-observations, which are later used for optimal interpolation. This procedure reduces correlations between observations and minimizes processing time.

Bias correction for past SST observation reports is based on Folland and Parker (1995). Observation data quality control is performed by checking ship tracks, dates and positions applicable to reports, and erroneous information is automatically corrected in the compilation of marine meteorological data at JMA. Based on observation data deviations from 1950−2000 normals for three months including the day of interest, the biases of data with identical ship call signs are estimated, and signs associated with large data biases are automatically blacklisted through daily analysis. Daily (final) analysis is performed with a delay of 31 days from real time to include delayed observations. Daily analysis for the latest 30-day period following the final analysis is also performed for real-time utilization. A detailed report on data characteristics is provided (Japan Meteorological Agency 2006).

COBE2 (updated from COBE) has been operational since May 2021 with an SST component (COBE-SST2) for use in century-scale monitoring of global warming and historical oceanic analysis. The main improvements from COBE to COBE2 are as follows:

1. The historical database of in-situ observations has been updated from ICOADS 2.0 (Woodruff *et al.* 1998) to 2.5 (Woodruff *et al.* 2011).

2. A new bias correction method enables estimation for the biases of individual SST measurement types, such as insulated/uninsulated buckets and engine-room intake. The bias of observations with no measurement type information is defined as a mixture of those of specified measurement types.

3. An updated method of estimating SSTs in ice-covered regions enables clearer statistical relations between sea-ice concentration and SSTs for consideration of freezing points in sea water as a function of climatological sea surface salinity.

4. A new SST analysis method includes construction of a daily SST field as a sum of the trend, interannual variations, and daily changes.

Daily updated COBE-SST2 data are used for:

1. Monitoring of long-term change in global average surface temperature anomalies.

2. Historical monitoring of equatorial SSTs in relation to phenomena such as El Niño/ La Niña and the Indian Ocean Dipole up to May 2015.

3. Input for the Japanese Reanalysis for Three Quarters of a Century (JRA-3Q; Kosaka *et al.* 2024; Section 2.11) covering the period from September 1947 to May 1985.

4. Input for the Japanese Reanalysis for Three Quarters of a Century with COBE-SST2 (JRA-3Q-COBE; Kosaka *et al.* 2024; Section 2.11) covering the period from June 1985 to December 1990.

5. Input for operational and historical oceanic analysis using Ocean Data Assimilation System data (MOVE/MRI.COM-G3; Fujii *et al.* 2023; Section 5.3).

Monthly average COBE-SST2 data are available on the TCC website[1] and the NEAR-GOOS Regional Real Time Database[2].

5.3 Ocean Data Assimilation and Prediction Systems

JMA has operated multiple ocean data assimilation systems based on the unified Multivariate Ocean Variational Estimation/Meteorological Research Institute Community Ocean Model (MOVE/MRI.COM) framework developed by its Meteorological Research Institute (MRI) since 2008. Currently, two such systems, MOVE-G3 and MOVE-JPN are in operation. MOVE-G3 is used to analyze the global ocean for El Niño monitoring and initialization of the oceanic part of the coupled seasonal prediction system (CPS3, Section 3.4). MOVE-JPN is used for analysis and prediction of oceanographic sub-mesoscale events and sea ice conditions over coastal areas around Japan. The MOVE/MRI.COM framework and the two operational systems are outlined below.

---

[1] https://www.data.jma.go.jp/tcc/tcc/products/elnino/cobesst2/cobe-sst2.html
[2] https://www.data.jma.go.jp/goos/data/database.html

5.3.1 Ocean General Circulation Model and Objective Analysis Scheme: Common Framework

MOVE/MRI.COM consists of an ocean general circulation model (MRI.COM) and an objective analysis scheme (MOVE). Although MRI.COM and MOVE are continuously developed with a variety of features, this subsection outlines only features adopted in the operational systems. With the increasing number of options available in both components, operational configurations depend on resolution and system objectives (Table 5.3.1).

MRI.COM (Tsujino *et al.* 2010, 2017; Sakamoto *et al.* 2023) is a general-purpose ocean model with an Arakawa B-grid arrangement by which primitive equations are solved under hydrostatic and Boussinesq approximations. The z^* vertical coordinate system (Adcroft and Campin 2004) that allows free surface elevation and shallow (< 10 m) bottom topography is used. For nonlinear momentum advection, a generalized enstrophy-preserving scheme (Arakawa 1972) and a scheme involving the concept of diagonally upward/downward mass momentum fluxes along a sloping bottom are applied. A tracer advection scheme based on conservation of second-order moments (Prather 1986) is adopted in most systems while the more lightweight QUICK (Leonard 1979) is adopted in the analysis models. The bottom boundary layer (Nakano and Suginohara 2002) adopted in the coarse global models helps to reproduce the downslope advection of dense water. Vertical viscosity and diffusivity are determined using the Generic Length Scale scheme of Umlauf and Burchard (2003). A variety of options also exist in lateral mixing and viscosity parameterization. For coarse models that do not resolve eddies, isopycnal mixing (Redi 1982) and eddy-induced transport parameterized by Gent and McWilliams (1990) are used for tracers, and harmonic viscosity with the parameterization of Smagorinsky (1963) is used for momentum. For eddy-permitting and finer models, a biharmonic operator is used for horizontal turbulent mixing, and biharmonic friction with Smagorinsky-like viscosity (Griffies and Hallberg 2000) is used for momentum. A sea ice model with the thermodynamics of Mellor and Kantha (1989), thickness categories, and ridging/rheology following the Los Alamos sea ice model (CICE, Hunke and Lipscomb 2006) is enabled in all operational systems. Surface forcing to drive the model is based on the Japanese Reanalysis for Three Quarters of a Century (JRA-3Q, Kosaka *et al.* 2024), the Global Spectral Model (GSM, Yonehara *et al.* 2023, Sections 2.5 and 3.2), and the Global Ensemble Prediction System (GEPS, Ota *et al.* 2023, Section 3.3), depending on lead times and other considerations. River runoff climatology is commonly added to freshwater flux, and tidal forcing is enabled in coastal monitoring models.

Variational analysis with vertically coupled Temperature-Salinity (T-S) Empirical Orthogonal Function (EOF) modal decomposition (Fujii and Kamachi 2003b) is the basis for all assimilation systems. The model domain is divided into several subregions for which vertical T-S EOF modes are calculated in advance from observed T-S profiles. The amplitudes of T-S EOF modes, which are proportional to T-S increments down to 2000 m, serve as control variables. The vertical correlation of background error is naturally expressed in EOF modes, whereas horizontal correlations are expressed with different lengths prescribed for individual subregions and may be anisotropic. With the tangent linear and adjoint models of MRI.COM, MOVE now has a four-dimensional variational (4DVAR) analysis capability (Usui *et al.* 2015) in addition to the more traditional three-dimensional variational analysis with first guess at appropriate time (3DVAR-FGAT, Lorenc and Rawlins 2005). Control variables are optimized via a quasi-Newtonian approach (Fujii and Kamachi 2003a; Fujii 2005), and the analysis results are used for the model temperature and salinity fields via incremental analysis updates (IAU, Bloom *et al.* 1996). IAU is also used to adjust forecast-model T-S fields to those of the analysis model (which may differ in horizontal resolution or tidal forcing) in a process known as the replay method or dynamical downscaling.

MOVE/MRI.COM assimilates satellite altimeter data and in-situ observations of temperature and salinity reported from ships, profiling floats, and moored/drifting buoys via GTS and other communication systems. The satellite altimeter data are the level-3 product from the Copernicus Marine Environment Monitoring Service (CMEMS)[3]. Data from objective sea surface temperature analysis (MGDSST (Kurihara *et al.* 2006, Subsection 5.2.1), performed independently from MOVE/MRI.COM) are also assimilated. MOVE can additionally assimilate sea ice concentration data with 3DVAR (Toyoda *et al.* 2011, 2016) and nudging. Daily objective analysis of sea ice concentration from space-based SSM/I sensors (Matsumoto *et al.* 2006) and sea ice concen-

---

[3]Product identifier: SEALEVEL_GLO_PHY_L3_NRT_OBSERVATIONS_008_044 (https://doi.org/10.48670/moi-00147)

Table 5.3.1: MRI.COM and MOVE options adopted in operational ocean data assimilation systems.

Operational system	MOVE-G3		MOVE-JPN				
			Analysis		Prediction		
Subsystem/Model	G3A	G3F	GLB	NPR	GLB	NP	JPN
MRI.COM major version	4	4	4	4	5	5	5
Horizontal tracer advection							
QUICK	Y			Y			
Second-order moment		Y	Y		Y	Y	Y
Bottom boundary layer	Y		Y		Y		
Lateral diffusion/viscosity parameterization							
Isopycnal diffusion	Y		Y		Y		
Gent and McWilliams	Y		Y		Y		
Harmonic viscosity	Y		Y		Y		
Biharmonic diff./visc.		Y		Y		Y	Y
Forcing							
JRA-3Q	Y	Y	Y	Y			
Global Analysis (GA)	Y	Y					
GSM			Y	Y	Y	Y	Y
GEPS					Y	Y	
Tides					Y	Y	Y
Temperature and salinity analysis							
3DVAR-FGAT			Y				
4DVAR	Y			Y			
IAU initialization (to analysis)		Y			Y	Y	Y
Assimilated SST product							
MGDSST	Y		Y	Y			
Sea ice concentration analysis							
3DVAR	Y	Y					
Nudging				Y		Y	Y
Use of SSM/I obj. anl.	Y	Y		Y		Y	
Use of manual analysis							Y

tration subjectively estimated on the basis of data from satellites, aircraft, ships and coastal observations are also assimilated.

5.3.2 Ocean Data Assimilation System for Global Oceans (MOVE-G3)

Table 5.3.2: MOVE-G3 specifications

|	
Horizontal grid spacing	G3A: 1° longitude × 0.3 − 0.5° latitude
	G3F: 0.25°
Vertical levels	60 (G3A with bottom boundary layer)
Number of grids	G3A: $364 \times 366 \times 61 = 8,126,664$
	G3F: $1,444 \times 676 \times 60 = 58,568,640$
Sea surface forcing	Radiative heat flux, precipitation, surface wind, pressure, temperature, humidity
	Delayed analysis: from JRA-3Q
	Early analysis: from Global Analysis
River runoff	Climatology from JRA55-do (Tsujino et al. 2018)
Assimilation	G3A: 4DVAR with 10-day windows (observations for the last 5 days assimilated by giving
	T-S increments for the first 5 days)
Initialization	G3F: IAU for 5 days using G3A results
Sea ice assimilation	3DVAR
Observational data	In-situ temperature and salinity above -2,000 m
	Sea level anomaly (Jason-3, Cryosat-2, Saral, Sentinel-3A, Sentinel-3B)
	Sea surface temperature (MGDSST) and sea ice concentration (SSM/I, Matsumoto et al. 2006)
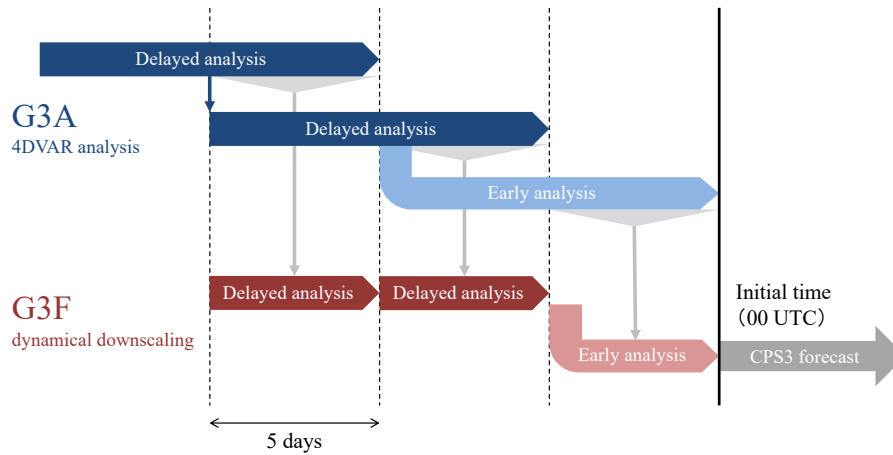
Figure 5.3.1: The MOVE-G3 system, with the abscissa representing the time of validity. Within a ten-day analysis window of the G3A subsystem, observations for the last five days are assimilated by giving T-S increments for the first five days, and restart files are created at the end of the fifth day. The G3F subsystem adjusts its five-day mean temperature and salinity fields to those of G3A using IAU (represented by downward grey triangles and arrows). Operationally, five mutually independent temporally staggered analysis streams are employed for daily initialization of the CPS3 coupled model (not shown).

Operation of the MOVE-G3 global ocean data assimilation system began in February 2022 (Table 5.3.2, Fujii et al. 2023) with incorporation of lower-resolution 4DVAR analysis (G3A) and initialization of oceanic parts for coupled forecasts (G3F, Figure 5.3.1). The G3A model adopts a horizontal resolution of 0.5° latitude and 1.0° longitude except for the 15°S – 15°N band, where latitudinal grid spacing is at a minimum of 0.3° between 6°S and 6°N, has 60 vertical levels and a bottom boundary layer (Nakano and Suginohara 2002),
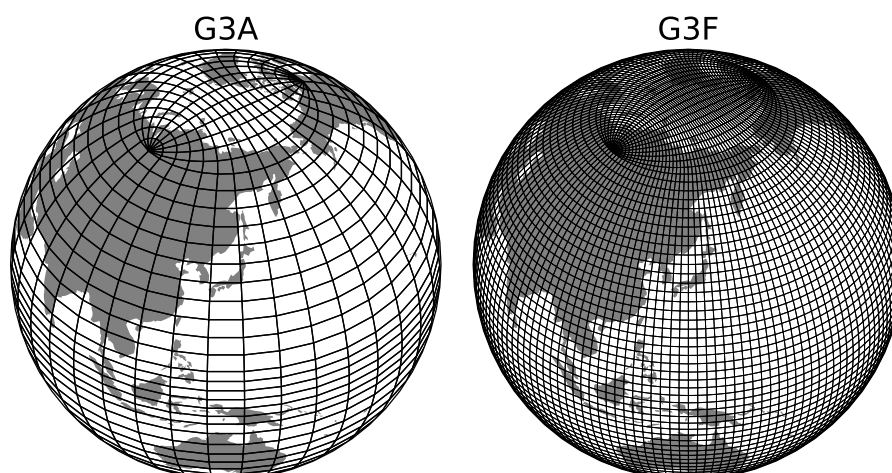
Figure 5.3.2: Tripolar coordinate adopted for the two MOVE-G3 models. Boundaries are shown for every 10 grids.

with 23 levels above 200 m, along with realistic bottom topography and a maximum depth of 6,300 m. The computational domain is the global ocean, including the Arctic Ocean with use of tri-polar horizontal coordinates (Figure 5.3.2). A bias correction scheme (Fujii *et al.* 2012) and a global water mass correction scheme (Kuragano *et al.* 2014) are incorporated into MOVE-G3. The G3F forecast model covers global oceans using a higher resolution of 0.25 degrees, initialized by downscaling G3A temperature and salinity fields with IAU.

Sea ice concentration is also assimilated in MOVE-G3 (Toyoda *et al.* 2011, 2016). The 3DVAR scheme first combines observation data from daily objective analysis of sea ice concentration (Matsumoto *et al.* 2006) with information on background sea ice concentration from the model forecast. The analysis concentration increment is then applied to gradually adjust model sea ice with IAU. No information on sea ice is passed from G3A to G3F, and concentration is assimilated independently in both.

Data production is enhanced to provide prompt and frequent initial conditions for the coupled model. Although MOVE-G3 has a five-day data window, five staggered analysis streams are applied so that initial conditions can be determined every day (valid at 00 UTC). The operational system features early analysis on the same day for initial conditions and delayed cycle analysis with a four-day delay for more uniform analysis. The early part involves the use of atmospheric Global Early Analysis with the GSM for surface forcing, whereas the delayed part involves the more uniform JRA-3Q. The 4DVAR system also generates ensemble perturbations approximating analysis error covariances using minimization histories (Niwa and Fujii 2020). With this capability, early analysis provides daily five-member initial ensembles for the coupled model.

MOVE-G3 output is used in various forms for JMA El Niño monitoring, and products for the equatorial Pacific region are published in Monthly Highlights on the Climate System and the El Niño Outlook. Report charts are also provided on the Tokyo Climate Center Web page[4].

5.3.3 Ocean Data Assimilation and Prediction System for the Seas Around Japan (MOVE-JPN)

MOVE-JPN consists of an analysis system that assimilates ocean observation data and simulates the latest ocean state, and a prediction system that initializes higher-resolution models based on analysis and forecasts ocean conditions.

The analysis system (Hirose *et al.* 2019, Table 5.3.3) consists of a global model (GLB) and a North Pacific

---

[4]https://www.data.jma.go.jp/tcc/tcc/index.html

model (NPR[5]), both with 60 levels, 31 of which are above 400 m. The GLB has a bottom boundary layer (Nakano and Suginohara 2002) and horizontal coordinates identical to those of G3A. The NPR model domain spans the area from 99°E to 75°W zonally and 15°S to 63°N meridionally. NPR horizontal resolution is variable, with values of 1/11° from 114°E to 163°E and 1/10° from 17°N to 56°N ($\approx$ 10 km around Japan) and coarser elsewhere. The NPR model (one-way nested within the GLB assimilating global data based on 3DVAR) assimilates observation data based on 4DVAR (Usui *et al.* 2015).

The MOVE-JPN prediction system consists of the GLB, another North Pacific model (NP) and the JPN model (Sakamoto *et al.* 2019, Table 5.3.4). The NP model domain is identical to that of NPR, but its horizontal resolution is zonally 1/11° and meridionally 1/10° over the entire domain (Figure 5.3.3). The JPN model domain spans the area 117−160°E and 20−52°N with grid spacing of around 2 km (zonally 1/33°, meridionally 1/50°). The JPN model is one-way nested to the two-way nested set of the GLB and NP models, all of which explicitly represent tidal motion. NP and JPN are initialized using the IAU scheme with temporal and spatial filtering on temperature and salinity fields from NPR 4DVAR analysis. Using surface boundary conditions output by the GSM, the JPN model forecasts ocean states around Japan with a lead time of 11 days. The two-way nested GLB and NP models continue to forecast ocean states for a month ahead based on GEPS and JRA-55 climatology forcing.

Table 5.3.3: MOVE-JPN analysis system specifications

Model domain	GLB: global
	NPR: 15°S − 63°N between 99°E and 75°W
Nesting	GLB/NPR 1-way off line
Horizontal grid spacing	GLB: 1° longitude × 0.3 − 0.5° latitude
	NPR: 1/11° longitude × 1/10° latitude for seas around Japan, coarser elsewhere
Vertical levels	60 (GLB with bottom boundary layer)
Number of grids	GLB: $364 \times 366 \times 61 = 8,126,664$
	NPR: $1,334 \times 578 \times 60 = 46,263,120$
Sea surface forcing	Radiative heat flux, precipitation, surface wind, pressure, temperature, humidity
	Delayed analysis: JRA-3Q
	Early analysis: GSM (Section 3.2)
River runoff	Climatology from JRA55-do (Tsujino *et al.* 2018)
Assimilation	GLB: 3DVAR with 5-day windows
	NPR: 4DVAR with 10-day windows (observations for the last 7 days assimilated by giving
	T-S increments for the first 3 days)
Sea ice assimilation	NPR: nudging
Observational data	In-situ temperature and salinity above -2,000 m
	Sea level anomaly (Jason-3, Cryosat-2, Saral, Sentinel-3a,b, HaiYang-2b)
	Sea surface temperature (MGDSST) and sea ice concentration (SSM/I, Matsumoto *et al.* 2006)

---

[5]The NPR model used for 4DVAR analysis is a reduced-resolution version of the NP model detailed later.
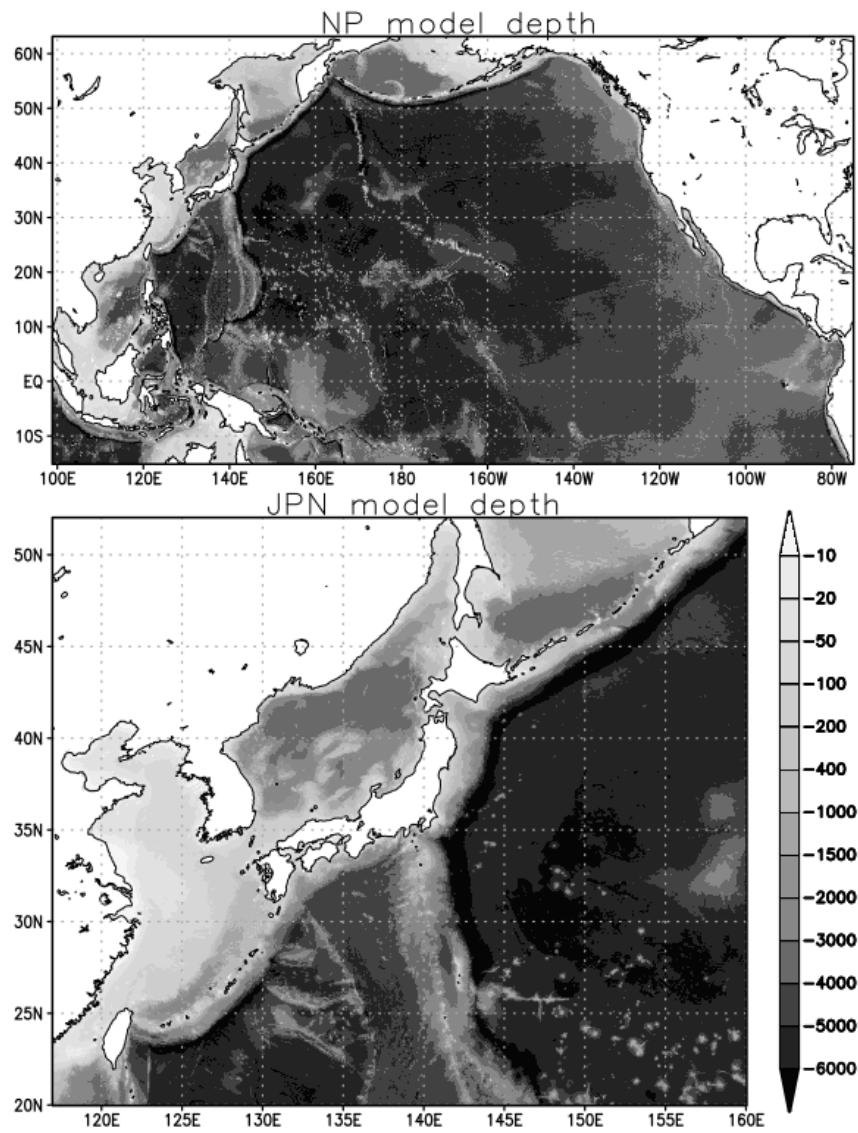
Figure 5.3.3: Bottom topography of the NP model (top) and the JPN model (bottom) in m. The figures show the domain of each model.

Table 5.3.4: MOVE-JPN prediction system specifications

Model domain	GLB: global
	NP: $15°S - 63°N$, $99°E - 75°W$
	JPN: $20° - 52°N$, $117° - 160°E$
Nesting	GLB and NP: 2-way on line
	JPN: 1-way off line to NP
Horizontal grid spacing	GLB: $1°$ longitude $\times$ $0.3 - 0.5°$ latitude
	NP: $1/11°$ longitude $\times$ $1/10°$ latitude
	JPN: $1/33°$ longitude $\times$ $1/50°$ latitude
Vertical levels	60 (GLB with bottom boundary layer)
Number of grids	GLB: $364 \times 366 \times 61 = 8,126,664$
	NP: $2,049 \times 784 \times 60 = 96,384,960$
	JPN: $1,423 \times 1,604 \times 60 = 136,949,520$
Tidal forcing	8 main tidal constituents
Sea surface forcing	Radiative heat flux, precipitation, surface wind, pressure, temperature, humidity
	Up to 11th day: GSM
	From 12th day: GEPS and JRA-55 climatology
River runoff	Climatology from JRA55-do (Tsujino *et al.* 2018)
Initialization	IAU for 3 days using GLB-3DVAR and NPR-4DVAR results
Sea ice initialization	NP: nudging to SSM/I
	JPN: nudging to JMA manual sea ice analysis
Prediction period	GLB and NP: 31 days
	JPN: 11 days

Table 5.4.1: Specifications of the Global Wave Model, the Coastal Wave Model and the Wave Ensemble System.

Model name	Global Wave Model	Coastal Wave Model	Wave Ensemble System
Type of wave model	spectral model (third-generation wave model, MRI-III)		
Area	global $75°N − 75°S$ $180°W − 0° − 180°E$	coastal sea of Japan $50°N − 20°N$ $120°E − 150°E$	global $75°N − 75°S$ $180°W − 0° − 180°E$
Grid size	$0.25° × 0.25°$ ($1440 × 601$)	$0.05° × 0.05°$ ($601 × 601$)	$0.5° × 0.5°$ ($720 × 301$)
Time step (advection term) (source term)	5 minutes 15 minutes	1 minute 3 minutes	10 minutes 30 minutes
Forecast range (initial time)	132 hours (06 and 18 UTC) 264 hours (00 and 12 UTC)	132 hours (00, 06, 12 and 18 UTC)	264 hours (00 and 12 UTC)
Spectral component	900 components 25 frequencies from 0.0375 to 0.3 Hz (logarithmically partitioned) 36 directions		
Initial condition	Analysis by Optimal Interpolation		
Boundary condition		Global Wave Model	
Wind field	Global Spectral Model (GSM)		Global Ensemble Prediction System (GEPS)
	Fujita's empirical formula and a corresponding gradient wind for a typhoon		
Shallow-water effects	Refraction and bottom friction		

5.4 Ocean Wave Models

5.4.1 Introduction

The Japan Meteorological Agency (JMA) operates the Global Wave Model (GWM), the Coastal Wave Model (CWM), and the Wave Ensemble System (WENS). The Shallow-water Wave Model (SWM) is also operated in selected regions.

The GWM, CWM and WENS are based on MRI-III developed by JMA's Meteorological Research Institute (Ueno and Kohno 2004). The current versions of the GWM and the CWM, which incorporate shallow water effects, have been used for short-range forecasting since May 2017. The WENS, which is a prediction system incorporating probability information for mid-range forecasts, has been in operation since June 2016. The specifications of the three models are given in Table 5.4.1, and their domains are shown in Figure 5.4.1.

The SWM is based on the WAM (The WAMDI Group 1988) with modification by the National Institute for Land and Infrastructure Management of the Ministry of Land, Infrastructure, Transport, and Tourism (MLIT), with quasi-operation under a cooperative framework with MLIT's Water and Disaster Management Bureau. It has a high resolution of 1 minute (see Table 5.4.2), and is operated over 22 areas. SWM products are used exclusively within JMA and MLIT's Regional Development Bureaus.

5.4.2 Ocean Wave Model Structure

The ocean wave models forecast the wave energy density (spectrum) of each frequency and direction (i.e., the two-dimensional (directional) wave spectrum). The basic equation is the energy balance expression:

$$\frac{\partial F}{\partial t} + \nabla \cdot (C_g F) + \frac{\partial}{\partial \theta}(\Omega F) = S_{net} = S_{in} + S_{nl} + S_{ds} + S_{btm} \tag{5.4.1}$$

where

$$\Omega = \frac{C_g}{C_p}\left(-\frac{\partial C_p}{\partial x}\cos\theta + \frac{\partial C_p}{\partial y}\sin\theta\right)$$

which represents refraction in shallow water. $F(f, \theta, x, t)$ is a two-dimensional spectrum, where f is the frequency and θ is the wave direction, $C_g(f, \theta, x)$ is the group velocity, and $C_p(f, x)$ is the phase speed. The
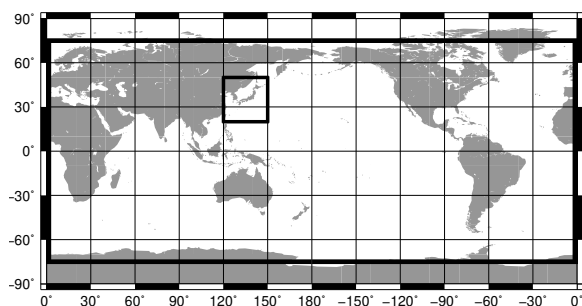
Figure 5.4.1: Calculation areas for the Global Wave Model and the Wave Ensemble System (outer thick lines), and the Coastal Wave Model (inner thick lines).
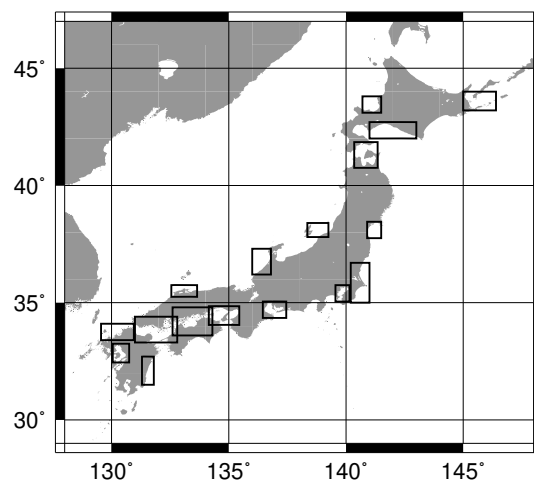

Figure 5.4.2: Calculation areas for the Shallow-water Wave Model.

Table 5.4.2: Specifications of the Shallow-water Wave Model.

Type of wave model	spectral model (third-generation wave model, WAM)					
Areas	Domain name	Grid size	Integration domain	Domain name	Grid size	Integration domain
	Tokyo Bay	37×43	$35.75°N - 35.05°N$ $139.55°E - 140.15°E$	Off Shimane	67×31	$35.75°N - 35.25°N$ $132.55°E - 133.65°E$
	Ise Bay	61×43	$35.05°N - 34.35°N$ $136.45°E - 137.45°E$	Ishikari Bay	49×43	$43.80°N - 43.10°N$ $140.70°E - 141.50°E$
	Harima-Nada Osaka Bay	79×49	$34.85°N - 34.05°N$ $134.15°E - 135.45°E$	Off Ishikawa	49×67	$37.30°N - 36.20°N$ $136.00°E - 136.80°E$
	Ariake Sea Shiranui Sea	43×49	$33.25°N - 32.45°N$ $130.05°E - 130.75°E$	Off Nemuro	85×49	$44.00°N - 43.20°N$ $145.00°E - 146.40°E$
	Off Niigata	55×37	$38.40°N - 37.80°N$ $138.35°E - 139.25°E$	Off Miyazaki	31×73	$32.70°N - 31.50°N$ $131.30°E - 131.80°E$
	Sendai Bay	37×43	$38.45°N - 37.75°N$ $140.90°E - 141.50°E$	Tsugaru Strait	61×67	$41.85°N - 40.75°N$ $140.35°E - 141.35°E$
	Off Tomakomai	121×43	$42.70°N - 42.00°N$ $141.00°E - 143.00°E$	Off Ibaraki Off Boso	49×103	$36.70°N - 35.00°N$ $140.20°E - 141.00°E$
	Suo-Nada Iyo-Nada Aki-Nada	109×67	$34.40°N - 33.30°N$ $131.00°E - 132.80°E$	Genkai-Nada	83×43	$34.10°N - 33.40°N$ $129.55°E - 130.95°E$
	Hiuchi-Nada	103×73	$34.80°N - 33.60°N$ $132.60°E - 134.30°E$			
Grid resolution	$1' \times 1'$					
Time step (advection term) (source term)	1 minute 1 minute					
Forecast range	39 hours					
Spectral component	1260 components 35 frequencies from 0.0418 to 1.1 Hz (logarithmically partitioned) 36 directions					
Initial condition	Coastal Wave Model					
Boundary condition	Coastal Wave Model					
Wind field	Meso-Scale Model (MSM)					
	Fujita's empirical formula and a corresponding gradient wind for a typhoon					

magnitude of group velocity is simply $C_g(f)$ for deep-water waves, and depends on water depth for shallow-water waves. S_{net} is a net source function consisting of S_{in}, S_{nl}, S_{ds}, and S_{btm}, which are briefly outlined below. Only the model numerics of the MRI-III are described here, as those of the WAM are already extensively referenced elsewhere (e.g. Janssen 2004).

1. S_{in}: energy input from wind. This value generally takes the form $S_{in} = A + BF$, where A is linear wave growth and BF is exponential growth. In the MRI-III, the formula of Cavaleri and Rizzoli (1981) is used for linear growth

$$A = 1.5 \times 10^{-3} \left(\frac{u_*^4}{2\pi g^2} \right) \exp\left[-\left(\frac{f_{PM}}{f} \right)^4 \right] (\max\{0, \cos(\theta - \theta_W)\})^4 \tag{5.4.2}$$

where u_* is the friction velocity of wind, θ_W is the wind direction, and g is the gravitational acceleration. In general, the linear term has little influence on wave growth except in the very early stages. Meanwhile, the exponential term BF has a key role in wave growth. In the MRI-III, The B is expressed as

$$B(f, u_*, \theta_W - \theta) = c_{in} \left(\frac{u_*}{C_{pd}} \right)^2 f \frac{\cos^3(\theta_W - \theta)}{|\cos(\theta_W - \theta)|} \tag{5.4.3}$$

where C_{pd} is the phase speed of deep water waves, i.e., $C_{pd} = \dfrac{g}{\omega} = \dfrac{g}{2\pi f}$.

This expression is based on Mitsuyasu and Honda (1982) and Plant (1982).

2. S_{nl}: nonlinear energy transfer associated with resonant interaction. Since rigorous calculation is highly time-consuming, a practical scheme known as discrete interaction approximation (DIA) (Hasselmann et al. 1985) is commonly used in operational wave models. This approach involves the use of only one parameter for the set of four resonant waves:

$$\left. \begin{array}{l} f_1 = f_2 = f, \\ f_3 = f(1 + \lambda) = f_+, \\ f_4 = f(1 - \lambda) = f_-, \\ \theta_1 = \theta_2 = \theta, \\ \theta_3 - \theta = \pm \cos^{-1} \left\{ \dfrac{1 + 2\lambda + 2\lambda^3}{(1 + \lambda)^2} \right\}, \\ \theta_4 - \theta = \mp \cos^{-1} \left\{ \dfrac{1 - 2\lambda - 2\lambda^3}{(1 - \lambda)^2} \right\} \end{array} \right\} \tag{5.4.4}$$

$$\left\{ \begin{array}{c} \delta S_{nl} \\ \delta S_{nl}^+ \\ \delta S_{nl}^- \end{array} \right\} = \left\{ \begin{array}{c} -2\dfrac{\varDelta f \varDelta \theta}{\varDelta f \varDelta \theta} \\ \dfrac{(1 + \lambda)(\varDelta f \varDelta \theta)}{\varDelta f_+ \varDelta \theta} \\ \dfrac{(1 - \lambda)(\varDelta f \varDelta \theta)}{\varDelta f_- \varDelta \theta} \end{array} \right\}$$

$$\times C f^{11} g^{-4} \left[F^2 \left\{ \frac{F_+}{(1 + \lambda)^4} + \frac{F_-}{(1 - \lambda)^4} \right\} - 2 \frac{F F_+ F_-}{(1 - \lambda^2)^4} \right] \tag{5.4.5}$$

$$S_{nl} = \delta S_{nl} + \delta S_{nl}^+ + \delta S_{nl}^- \tag{5.4.6}$$

where $F \equiv F(f, \theta)$, $F_+ \equiv F(f_+, \theta_3)$, $F_- \equiv F(f_-, \theta_4)$. The coefficient C is determined to fit exact calculation for the JONSWAP spectrum. Hasselmann et al. (1985) defined the related parameters as $\lambda = 0.25$, corresponding to $\theta_3 - \theta = \pm 11.5°$, $\theta_4 - \theta = \mp 33.6°$ and $C = 3 \times 10^7$. DIA calculation is found to support highly accurate estimation if multiple parameters are combined. δS_{nl} is the rate of change in nonlinear energy transfer for the parameter λ. δS_{nl}, δS_{nl}^+ and δS_{nl}^- are calculated with three configurations in the MRI-III. The parameters used are $\lambda_1 = 0.19\,(C_1 = 1.191 \times 10^7)$, $\lambda_2 = 0.23\,(C_2 = 6.835 \times 10^6)$, and $\lambda_3 = 0.33\,(C_3 = 1.632 \times 10^6)$.

3. S_{ds}: energy dissipation associated with wave breaking and other effects. In the MRI-III, dissipation terms are expressed as local energy dissipation as proposed by Ueno (1998).

$$S_{ds} = -c_b \frac{u_*}{g^3} f^7 \left(F(f, \theta) \right)^2 \tag{5.4.7}$$

where c_b is a coefficient determined to fit wave generation. In the MRI-III, a slightly artificial swell decay process is included.

$$S_{sds} = -2.96 \times 10^{-6} \tanh \left[4 \frac{f_s - f}{f_p} \right] F(f, \theta) \tag{5.4.8}$$

where $f_p = 0.156g/U_{10N}$ represents the peak frequency of the Pierson-Moskowitz (PM) spectrum from the 10m height wind speed U_{10N}. This decay function is applied to the spectrum of frequencies lower than $f_s = 1.8 f_p$ when the significant wave height exceeds 1.5m.

4. S_{btm}: the energy loss associated with bottom friction. This effect needs to be considered for shallow water. In the MRI-III, this term is taken from Hasselmann *et al.* (1973).

$$S_{btm} = -\frac{0.038}{g^2} \cdot \frac{(2\pi f)^2}{\sinh^2(kd)} \cdot F(f, \theta) \tag{5.4.9}$$

where k is the wave number and d is depth. Energy loss increases for shallow water and long-period waves.

5.4.3 Wind Field

Wind fields for the GWM and the CWM are given by the Global Spectral Model (GSM), while the SWM uses Meso-Scale Model (MSM) winds. For the WENS, 51-member wind fields of the Global Ensemble Prediction System (GEPS) are employed.

Wind fields around typhoons are empirically modified in the GWM, CWM and SWM. As typhoons generate extremely high waves in the western North Pacific, accurate wave forecasting is crucial to maritime and coastal safety. As NWP models may not adequately predict typhoon intensity or tracks, wind fields based on operational typhoon analysis and forecasting are imposed onto NWP winds (known as bogus winds) when a typhoon is present over the western North Pacific. Wave conditions may differ significantly with changes in typhoon track, especially in the limited region covered by the SWM. Accordingly, wave fields are also predicted with the assumption of five different paths for each approaching typhoon (center, faster, slower, and right/left of forecast circle) within forecast error circles. See Subsection 5.5.1.3 for a description of forecast circles.

To create bogus wind data, sea level pressure distribution near a typhoon is assumed to have a profile expressed by Fujita's empirical formula (Fujita 1952)

$$P(r) = P_\infty - \frac{P_\infty - P_0}{\sqrt{1 + (r/r_0)^2}} \tag{5.4.10}$$

where P_∞, P_0 and r_0 denote the ambient pressure, the central pressure of the typhoon, and the scaling factor of the radial distribution of the pressure, respectively. Surface winds near the typhoon are estimated from the pressure field by assuming the gradient wind balance with modifications based on the typhoon movement and surface friction effects.

5.4.4 Wave Analysis

An assimilation scheme (Kohno *et al.* 2012) for the GWM and the CWM was introduced in October 2012. In these models, initial conditions (wave spectra) are modified based on significant wave heights under the Objective Wave Analysis System (OWAS) (Kohno *et al.* 2009), which is used for objective analysis of wave heights using optimal interpolation (OI) with observations from radar altimeters on board satellites, buoys and coastal wave recorders, and ship reports (Table 5.4.3). Data assimilation improves the prediction of ocean wave fields, especially in terms of shorter forecast times and swell propagation.

Table 5.4.3: JMA Objective Wave Analyses System specifications.

Analysis scheme	Optimal interpolation
Data cut-off time	6 hours and 25 minutes for early run analysis
	12hours for delayed analysis
First guess	6-hour forecast by the GWM and the CWM
Analysis variables	Significant wave height
Grid size	0.25°×0.25° grid for the GWM,
	0.05°×0.05° grid for the CWM
Domain	Global oceans for the GWM,
	Coastal sea of Japan for the CWM
Observational data	0.25°×0.25° grid super-observational data from BUOY, SHIP, Nowphas, GPS wave meter, Jason-3,
	SARAL, and Sentinel-3A/B
Assimilation window	6 hours

5.4.5 Products

JMA provides various ocean wave products based on model data via its website[6].

Such output based on GWM information comes from RSMC activities for numerical ocean wave prediction.

Charts showing analysis and 24-hour ocean wave forecasts are provided twice a day via the JMH radio facsimile broadcast service and the JMA website for the Western North Pacific and seas around Japan (Figure 5.4.3). The charts indicate significant wave heights, peak wave directions and peak wave periods. In addition, information on rough sea areas that may hinder maritime navigation was incorporated for forecast charts in 2017. The horizontal hatching in Figure 5.4.3 (a) indicates areas of crossing waves that may give rise to unexpectedly high-sea conditions. The vertical hatching in Figure 5.4.3 (b) indicates areas of increased wave height and steepness due to the effects of opposing ocean currents.

The following probabilistic medium-range forecast products highlighting significant wave heights and periods are statistically produced from WENS predictions:

1. Distribution maps for ensemble mean, maximum, 3rd quartile, probability of threshold breaches and ensemble spread of elements for ocean wave forecasts

2. Time-series representations with box plots and probability of threshold breaches

These products are provided on JMA's website for the WMO Severe Weather Forecasting Programme (SWFP[7]) and on the Numerical Typhoon Prediction (NTP) website for Typhoon Committee members. Figure 5.4.4 and Figure 5.4.5 show examples for TY Surigae (2102).

---

[6]https://www.jma.go.jp/jma/en/NMHS/JMA_RSMC.html
[7]https://www.wis-jma.go.jp/swfdp/
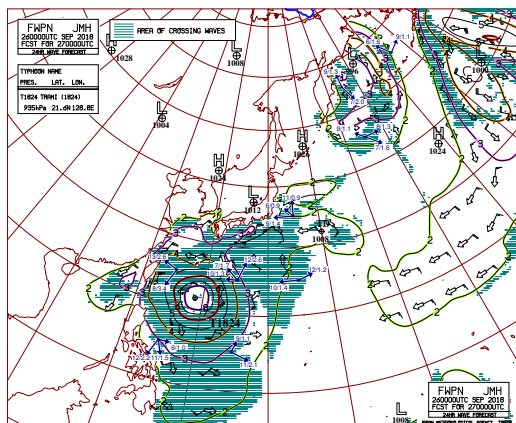
(a) Wave forecast chart for the Western North Pacific (FWPN) created from the GWM.
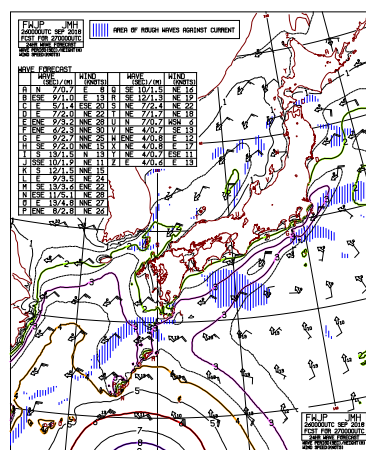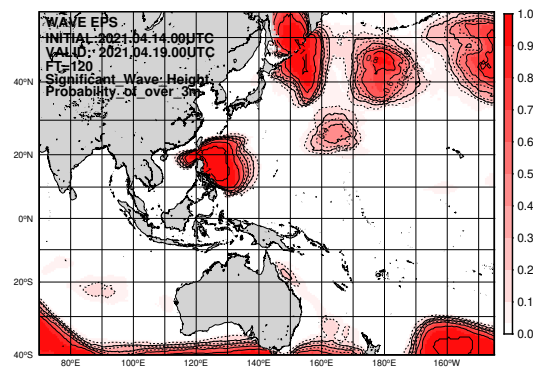

(b) Wave forecast chart for coastal regions of Japan (FWJP) created from the CWM.

Figure 5.4.3: Wave forecast charts based on 24-hour model predictions with an initial time of 00 UTC on 26 September 2018, including significant wave height(contours), wave direction(arrows), sea surface wind speed and direction(barbs).
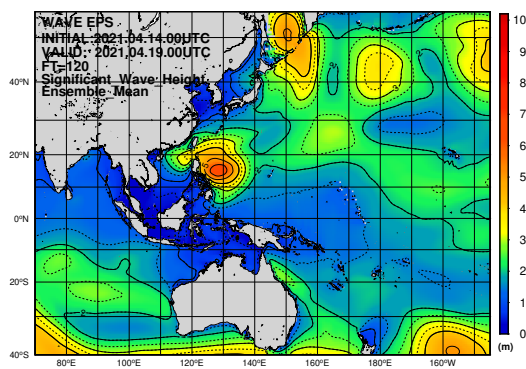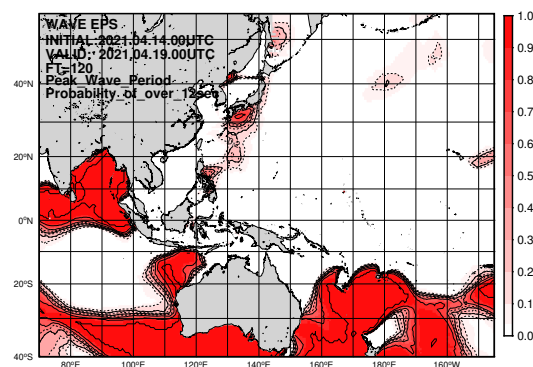

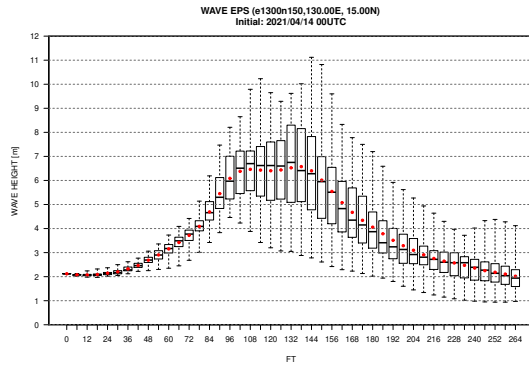(a) Ensemble means of significant wave heights.

(b) Probability of wave heights over 3 m.
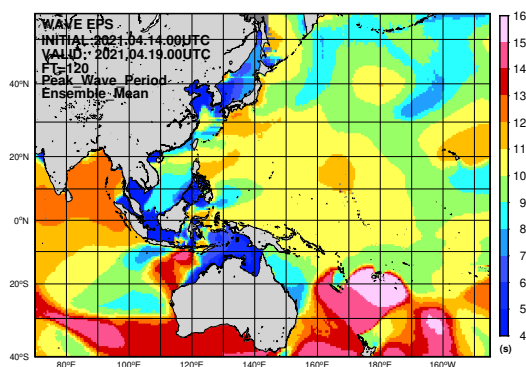
(c) Ensemble means of wave periods.

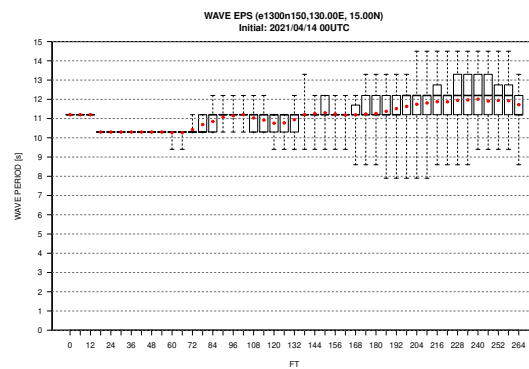(d) Probability of wave periods over 12 sec.

Figure 5.4.4: Distribution maps from 120-hour WENS predictions with an initial time of 00 UTC 14 on April 2021.
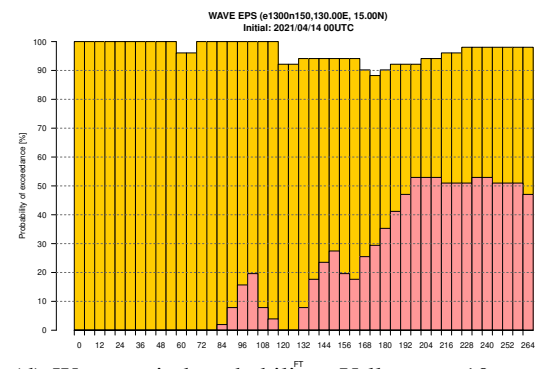
(a) Box plots for significant wave heights.
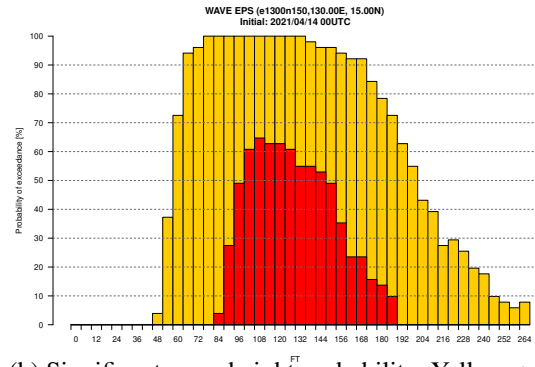
(b) Significant wave height probability. Yellow: > 3 m; red: > 6 m.

(c) Box plots for wave periods.

(d) Wave period probability. Yellow: > 10 sec; pink: > 13 sec; red: > 15 sec.

Figure 5.4.5: Time-series representations for areas off the east coast of the Philippines from WENS prediction with an initial time of 00 UTC 14 on April 2021.

5.4.6 Improvement and Development

The main improvements made to JMA ocean wave models since 2017 are as follows:

1. The shallow water effect was introduced into the GWM and the CWM in 2017, and into the WENS in 2020.

2. WENS horizontal resolution was upgraded from 1.25° to 0.5° in 2020.

3. The number of WENS members was increased from 27 to 51 in 2021.

4. GWM horizontal resolution was enhanced from 0.5° to 0.25° in January 2023.

Figure 5.4.6 shows monthly root mean square errors (RMSEs) for the significant wave height of the GWM against all kinds of observations measured by buoys, ships and satellites from 2012 to 2022. The remarkable improvement of T+0 RMSE in late 2012 corresponds to the implementation of data assimilation. The gradual decrease in RMSEs for the all lead times suggests the improvement of the performance of the JMA's weather and wave prediction systems.
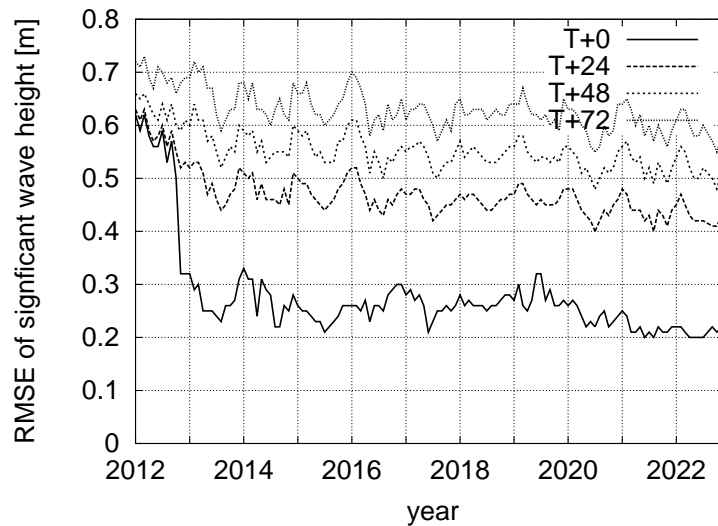

Figure 5.4.6: Time-series representation of analysis and forecast scores for the GWM.

Wave forecast errors are occasionally observed in relation to typhoons. For example:

1. Wave distribution resembling ball pairs sometimes appears due to the bogus wind embedding method.

2. As the model does not resolve the details of typhoon wind fields, especially in the extra-tropical stage, data on initial winds with bogus winds need to be improved.

5.5 Storm Surge Model

5.5.1 Japan-Area Storm Surge Model

5.5.1.1 Introduction

The Japanese Archipelago is vulnerable to storm surges because of its topography characterized by gulfs open to the south and shallow coasts, making accurate and timely forecasts/warnings crucial in mitigating related threats to life and property.

The Japan Meteorological Agency (JMA) is responsible for issuing storm surge warnings/advisories for the area, and has operated a numerical storm surge model since July 1998 to provide basic related information. The model was initially run four times a day whenever a typhoon was present in the vicinity, and has undergone enhancements including model domain enlargement, prediction of extratropical cyclone conditions, extension of forecast periods, and addition of advection terms. Since May 2010, a new storm surge model with higher resolution (approx. 1-km mesh near coastal areas) and gridded astronomical tide analysis have been implemented in storm tide calculation to produce even more practical information and warnings.

JMA also began providing information on the probability of warnings in 2017. This gave rise to the need for probabilistic prediction modeling specific to Japan for estimation of storm surge risk with a 3+ day lead time. To meet this demand, a new prediction system named Japan-area storm surge Probabilistic Forecast System (PFS; Subsection 5.5.1.6) was incorporated in August 2022.

5.5.1.2 Dynamics

Storm surges are mainly caused by the effects of wind setup due to strong onshore sea surface winds and inverse barometer effects associated with pressure drops in low-pressure systems. The effects of wind setup are proportional to the square of wind speed and inversely proportional to water depth, and are related to coastal topography, meaning that they are amplified in open bays against the wind.

The JMA storm surge model is similar to the one described in Higaki *et al.* (2009), and is based on two-dimensional shallow water equations driven by meteorological fields. These equations are composed of vertically integrated momentum equations in two horizontal directions:

$$\frac{\partial U}{\partial t} + u\frac{\partial U}{\partial x} + v\frac{\partial U}{\partial y} - fV = -g(D + \eta)\frac{\partial(\eta - \eta_0)}{\partial x} + \frac{\tau_{sx}}{\rho_w} - \frac{\tau_{bx}}{\rho_w} \tag{5.5.1a}$$

$$\frac{\partial V}{\partial t} + u\frac{\partial V}{\partial x} + v\frac{\partial V}{\partial y} + fU = -g(D + \eta)\frac{\partial(\eta - \eta_0)}{\partial y} + \frac{\tau_{sy}}{\rho_w} - \frac{\tau_{by}}{\rho_w} \tag{5.5.1b}$$

and the continuity equation:

$$\frac{\partial \eta}{\partial t} + \frac{\partial U}{\partial x} + \frac{\partial V}{\partial y} = 0 \tag{5.5.2}$$

where U and V are volume fluxes in the x- and y-directions, defined as:

$$U \equiv \int_{-D}^{\eta} u\,dz \tag{5.5.3a}$$

$$V \equiv \int_{-D}^{\eta} v\,dz \tag{5.5.3b}$$

Other notations are as follows. f is the Coriolis parameter; g is gravity acceleration; D is the water depth below mean sea level; η is surface elevation; η_0 is the inverse barometer effect converted into the equivalent water column height; ρ_w is the density of water; τ_{sx} and τ_{sy} are the x- and y-components of wind stress on the sea surface, respectively; and τ_{bx} and τ_{by} are the x- and y-components of the stress of bottom friction, respectively. As for the drag coefficient, adjusted parameterization is adopted in reference to the results of Smith and Banke (1975) and Frank (1984):

$$c_{\mathrm{d}} = \begin{cases} (0.63 + 0.1185W) \times 10^{-3} & (W < 20 \text{ m/s}) \\ \{3.00 + 0.0120(W - 25)\} \times 10^{-3} & (W \geq 20 \text{ m/s}) \end{cases} \tag{5.5.4}$$

where W is wind speed.

The equations are solved via numerical integration using the explicit finite difference method. A staggered (Arakawa-C) grid (Arakawa and Lamb 1977) is adopted for the grid system.

5.5.1.3   Meteorological Forcing

Dynamically predicted meteorological fields (surface wind and sea-level pressure) from the Meso-Scale Model (MSM) are used for external forcing to drive the storm surge model. Simple parametric TC model values (referred to here as typhoon bogussing) are also used for forcing when tropical cyclones (TCs) intensifying into typhoons are expected in the area around Japan.

The main purpose of typhoon bogussing is to predict storm surges based on official JMA typhoon forecasts, which are the most reliable at the time but not necessarily equivalent to those of the MSM. Single results remain inadequate for risk analysis because storm surges greatly depend on TC tracks. To take into account the influence of TC track uncertainty on storm surges, five runs of the storm surge model are conducted with potential TC tracks prescribed at the center of and at four points in the circle within which the TC is forecast to be with a probability of 70% (Figure 5.5.1). The five runs are (1) center track, (2) fastest track, (3) rightward-biased track, (4) slowest track, and (5) leftward-biased track. These data are used to create meteorological fields with the parametric TC model.
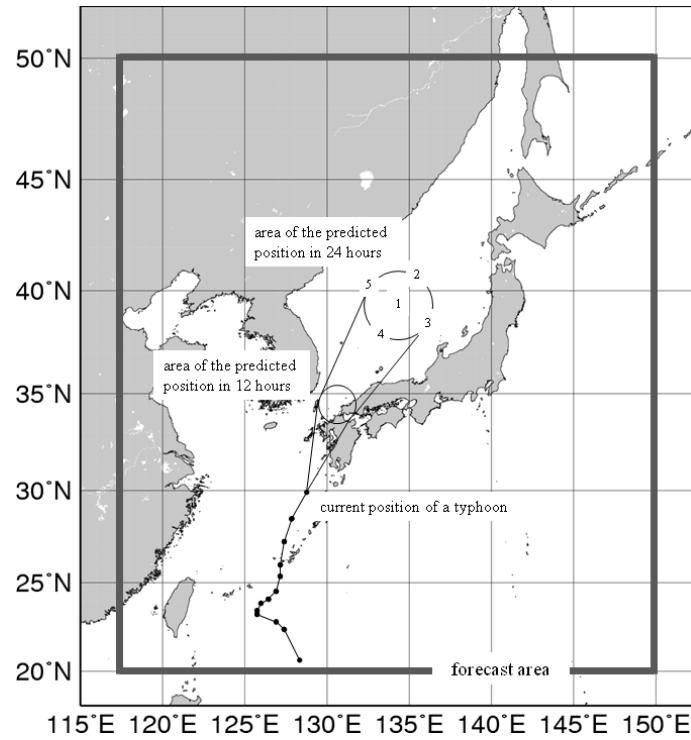

Figure 5.5.1: Tracks of typhoon bogussing and the domain of the Japan-area storm surge model

The typhoon bogussing utilizes Fujita's formula (Fujita 1952), which represents radial pressure distribution in a TC:

$$P = P_\infty - \frac{P_\infty - P_{\mathrm{c}}}{\sqrt{1 + (r/r_0)^2}} \tag{5.5.5}$$

217

and the gradient wind relation:

$$-\frac{v_g^2}{r} - f v_g = -\frac{1}{\rho_a}\frac{\partial P}{\partial r} \tag{5.5.6}$$

In Eq. (5.5.5), P is atmospheric pressure at distance r from the center of the TC, P_∞ is environmental pressure, P_c is the central pressure of the TC and r_0 is a scaling factor for radial distribution of pressure. In Eq. (5.5.6), ρ_a is the density of air and v_g is the gradient wind speed.

To represent the asymmetry of the wind field w in a TC, the moving velocity vector of the TC multiplied by a weight that decays exponentially with distance from the TC center is added to the gradient wind:

$$w = C_1 \left\{ v_g + C \cdot \exp\left(-\pi\frac{r}{r_e}\right) \right\} \tag{5.5.7}$$

C is the TC velocity vector, and r_e is the decay coefficient.

Moreover, an upwind directional land roughness parameterization of Westerink *et al.* (2008) is adopted to represent the wind speed reduction in coastal areas.

TC analysis and forecast information, such as the center position, central pressure and maximum wind, is applied to these formulas to synthesize the wind and pressure fields (Konishi 1995).

5.5.1.4 Model Specifications

Table 5.5.1 gives the specifications of the storm surge model, whose domain covers the whole of Japan (Figure 5.5.1).

Table 5.5.1: Japan-area storm surge model specification

Model	two-dimensional model
Grid	Lat-Lon Arakawa-C grid
Region	20°N - 50°N, 117.4°E - 150°E
Resolution	approximately 1, 2, 4, 8, 16 km (Adaptive mesh)
Boundary conditions	Modified radiation condition at open boundaries and zero normal flows at coastal boundaries
Time step	4 seconds
Initial time	00, 03, 06, 09, 12, 15, 18, 21 (UTC)
Forecast period	78 hours (00, 12 UTC) and 39 hours (03,06,09,15,18,21 UTC)
Member	TC case: 6 members (MSM+5 typhoon bogussing) no TC case: 1 member (MSM)

Since storm surge is essentially a long wave, its phase speed is proportional to the square root of water depth. It is thus inefficient to set the same resolution for all grids in consideration of computer resources. Accordingly, the Adaptive Mesh Refinement (Berger and Oliger 1984), in which the mesh is fine over shallow water and coarse over deep water, is adopted. The resolution is varied over five levels (1, 2, 4, 8 and 16 km) with water depth (Figure 5.5.2). This method makes storm surge calculation efficient, compared to the normal lat-lon grid system.

The storm surge model runs every three hours for forecasts up to 78 or 39 hours ahead. Initial conditions such as surface elevation (η) and volume fluxes (U and V) are created from the previous calculation using the latest MSM prediction as forcing (hindcasts). As these conditions are less important than those in atmospheric models, observation data are not assimilated.

The model computes only storm surges, i.e. anomalies from the level of astronomical tides. However, storm tides (storm surge plus astronomical tide) are required to issue storm surge warnings. Astronomical tides are predicted using harmonic analysis of sea level observations based on JMA's gridded astronomical tide method, in which astronomical tide calculation is performed even for no-observation grid areas (Subsection
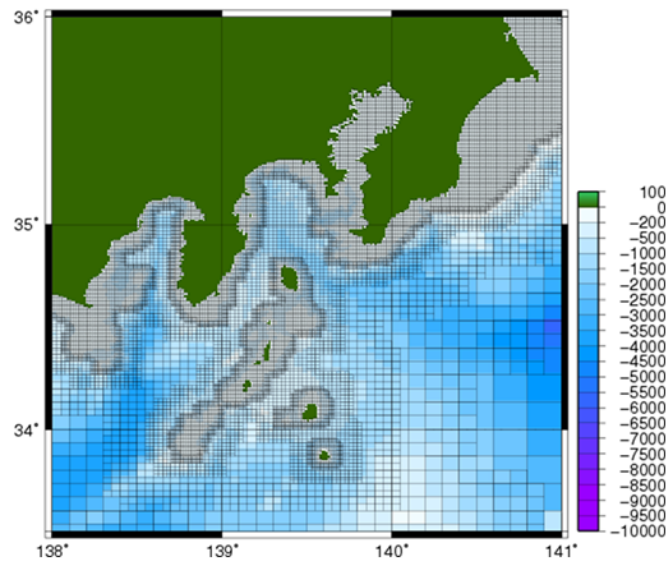
Figure 5.5.2: Storm surge model horizontal grid system and water depth (around the Kanto region)

5.5.3). After storm surge model computation, the astronomical tide level for the coastal area is linearly added to the predicted storm surge.

5.5.1.5 Verification

The accuracy of storm surge prediction depends on that of the storm surge model itself and atmospheric model conditions. To help eliminate forecast errors in atmospheric model input, the accuracy of the model was evaluated using storm surge predictions driven by atmospheric analysis data.

Figure 5.5.3 shows a scatter diagram of storm surge hindcasts against observation values from 210 tide stations for statistical periods of TC presence from 2019 to 2022. These stations are managed by organizations including JMA, the Ports and Harbours Bureau, the Japan Coast Guard and the Geospatial Information Authority of Japan. The figure shows prediction errors in the range of ± 50 cm, although large errors (exceeding observation by more than 50 cm) are also observed. These errors may be attributable to factors not considered in the storm surge model, such as wave setup, ocean currents and sea water stratification.

Storm surge associated with Typhoon Jebi (T1821) is presented here as an example of related prediction. Figure 5.5.4 shows the track of the typhoon, which passed over central Japan and caused storm surge conditions in Osaka Bay and elsewhere on 4 September 2018. Figure 5.5.5 (a) shows storm surge distribution around the bay as of 06 UTC on 4 September as predicted by the storm surge model, which reasonably forecasted the large surge behaviors associated with wind setup in the bay's inner part. Figure 5.5.5 (b) shows a time-series chart of storm surge at the port of Osaka. The peak was slightly underestimated and the forecast of its timing was delayed by about an hour, but in general the extreme storm surge conditions were fairly predicted.

5.5.1.6 Probabilistic Prediction

When TCs intensifying into typhoons are expected in the vicinity of Japan, the Japan-area storm surge model calculates predictions based on a potential ensemble system with six potential scenarios. As this number is insufficient for consideration of typhoon forecast uncertainties up to five days ahead, JMA developed a new Japan-area storm surge PFS that provides perturbations to TC tracks with reference to the Probabilistic storm Surge (P-Surge) model (Taylor and Glahn 2008; Gonzalez and Taylor 2018) operated by the National Hurricane Center (NOAA/NHC).
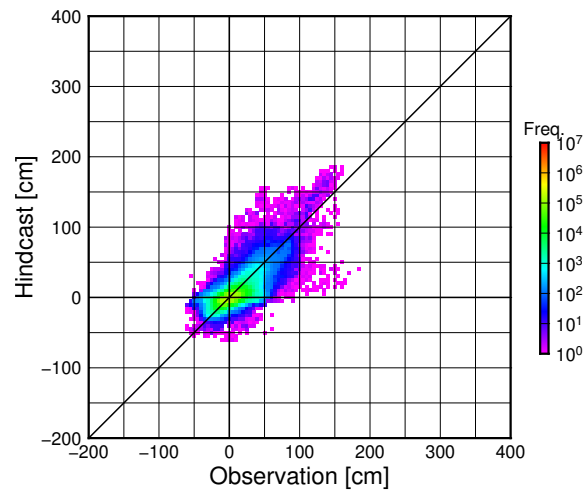
Figure 5.5.3: Scatter diagram of storm surge hindcast values against observed values
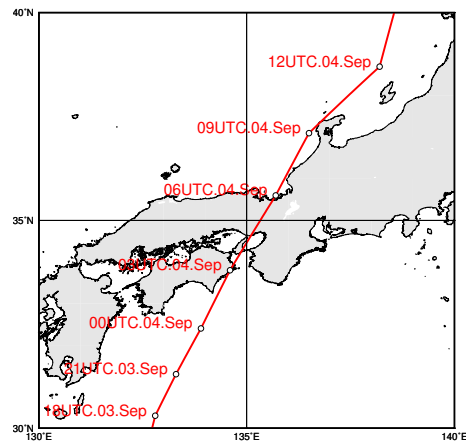

Figure 5.5.4: The track of Typhoon Jebi (T1821)

(a) Distribution of storm surge at 06 UTC on 4 September around Osaka Bay

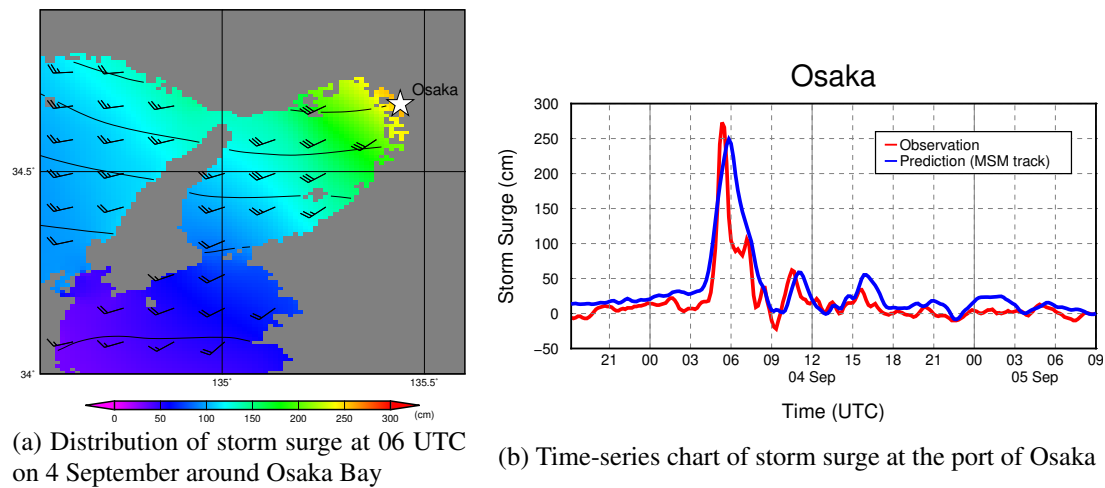(b) Time-series chart of storm surge at the port of Osaka

Figure 5.5.5: Storm surge distribution and time-series chart for the port of Osaka as predicted by the storm surge model with an initial time of 18 UTC on 3 September 2018

Most system specifications are common to those of deterministic modeling, with 21 members and no execution during non-TC periods. The PFS is driven only by typhoon bogussing as a meteorological forcing factor.

Figure 5.5.6 shows PFS track placement, with each member set with horizontal shifting of the official TC track at equal intervals. The overall tracks of cross-track members cover a 70% probability circle and an outer margin region. The PFS implants typhoon bogussing into 21 tracks and operates storm surge predictions up to 132 hours (5.5 days) ahead. In consideration of time-direction errors, prediction post-processing is implemented to create along-track members by shifting each PFS cross-track member with time interpolation in 21 ways to create 441 predictions. Figure 5.5.7 shows an example of such calculation for storm tide data at Osaka for Typhoon Jebi (T1821). In such cases, excesses in warning criteria can be predicted for some members.

Probabilistic prediction requires assignment of a probability density to each member. In the system, two-dimensional normal distribution is assumed for probability density distribution that TC center locations may assume with respect to typhoon forecast circles, with members closer the circle center being assigned higher probabilities. Based on probability densities of members overall, predictions of variables such as storm surge potential and storm tide percentiles are calculated, and products are created accordingly (see Figure 5.5.8).
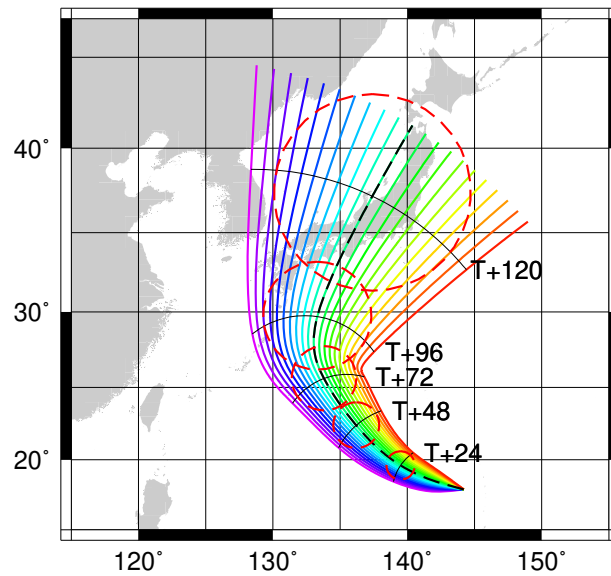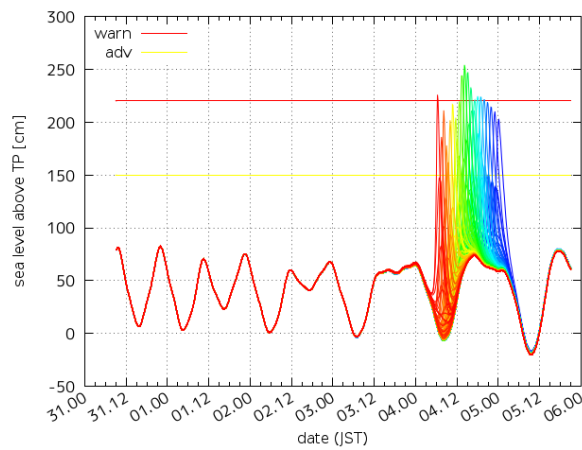
Figure 5.5.6: PFS member tracks

Figure 5.5.7: Time-series representation of storm tides at the port of Osaka based on PFS prediction with an initial time of 00 UTC on 31 August 2018
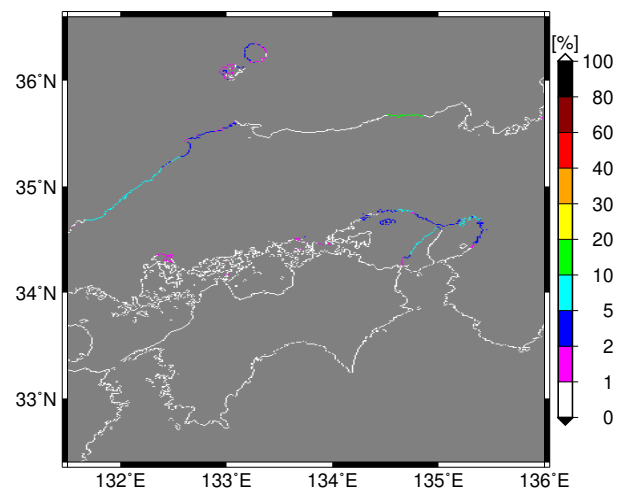

Figure 5.5.8: Excess probability in storm tide warning criteria on the fourth day based on PFS products with an initial time of 00 UTC on 2 September 2018

5.5.2 Asia-Area Storm Surge Model

5.5.2.1 Introduction

The late 2000s saw severe storm surge disasters worldwide, including on the coast of the Gulf of Mexico (caused by Hurricane Katrina) in 2005, on the coast of Bangladesh (caused by Cyclone Sidr) in 2007, and on the coast of Myanmar (caused by Cyclone Nargis) in 2008.

In response to a request by the WMO Executive Council (60th session, June 2008), WMO initiated the development of the regional Storm Surge Watch Scheme (SSWS) for areas affected by tropical cyclones. In relation to the western North Pacific and the South China Sea, the ESCAP/WMO Typhoon Committee (41st session, January 2009) endorsed a commitment by the RSMC Tokyo - Typhoon Center to produce storm surge forecasts with the aim of strengthening the storm surge warning capabilities of National Meteorological and Hydrological Services (NMHSs) in the region. JMA began development of a storm surge model for the Asia area in 2010 in collaboration with Typhoon Committee Members providing sea level observation and sea bathymetry data. Horizontal distribution maps of predicted storm surges and time-series charts are published on JMA's Numerical Typhoon Prediction website (Hasegawa *et al.* 2017).

In the last decade, Hurricane Sandy made landfall on the eastern coast of USA in 2012, causing serious damages including the traffic paralysis, massive blackouts and cessation of economic activity in New York. Typhoon Haiyan also caused more than 6,000 fatalities in the Philippines in 2013. Against such a background, storm surge and inundation countermeasures play pivotal roles in efforts to prevent typhoon-related disaster condition.

5.5.2.2 Dynamics

The basic equations for the Asia-area storm surge model are essentially the same as those for the Japan-area model (Subsection 5.5.1), with the exception of definition in a spherical coordinate system. The expressions incorporate vertically integrated momentum fluxes associated with the influence of the earth's rotation with gravity acceleration:

$$\frac{\partial U}{\partial t} + \frac{1}{R\cos\varphi}\left(\frac{\partial u^2 H}{\partial \lambda} + \frac{\partial uvH\cos\varphi}{\partial \varphi}\right) - fvH - \frac{uvH}{R}\tan\varphi = -\frac{gH}{R\cos\varphi}\frac{\partial(\eta-\eta_0)}{\partial \lambda} + \frac{\tau_{s\lambda}}{\rho_w} - \frac{\tau_{b\lambda}}{\rho_w} \quad (5.5.8a)$$

$$\frac{\partial V}{\partial t} + \frac{1}{R\cos\varphi}\left(\frac{\partial uvH}{\partial \lambda} + \frac{\partial v^2 H\cos\varphi}{\partial \varphi}\right) + fuH + \frac{u^2 H}{R}\tan\varphi = -\frac{gH}{R}\frac{\partial(\eta-\eta_0)}{\partial \varphi} + \frac{\tau_{s\varphi}}{\rho_w} - \frac{\tau_{b\varphi}}{\rho_w} \quad (5.5.8b)$$

and the continuity equation:

$$\frac{\partial \eta}{\partial t} + \frac{1}{R\cos\varphi}\left(\frac{\partial uH}{\partial \lambda} + \frac{\partial vH\cos\varphi}{\partial \varphi}\right) = 0 \quad (5.5.9)$$

Here, H is total depth, R is the earth's radius, and (λ, φ) are the zonal and meridional direction coordinates. Other values are as per those of the Japan-area storm surge model. Wind stress is expressed as:

$$\tau_{s\lambda} = c_d \rho_a W u_w \quad (5.5.10a)$$

$$\tau_{s\varphi} = c_d \rho_a W v_w \quad (5.5.10b)$$

where c_d is the drag coefficient, ρ_a is the density of air, $W \equiv \sqrt{u_w^2 + v_w^2}$ is the wind speed and (u_w, v_w) is the wind velocity. The drag coefficient is set based on the results of Peng and Li (2015):

$$c_d = \begin{cases} (3.146 - 0.00188 \times (W-33)^2) \times 10^{-3} & (W < 60 \text{ m/s}) \\ (1.5 + 0.2755 \times e^{-0.3685(W-60)}) \times 10^{-3} & (W \geq 60 \text{ m/s}) \end{cases} \quad (5.5.11)$$

5.5.2.3 Data

Bathymetry data for the Asia-area storm surge model come from 15-second-interval grid datasets of the General Bathymetric Chart of the Oceans (GEBCO 2021) (Figure 5.5.9).

Astronomical tides are determined via harmonic analysis with past tide observation data provided by Typhoon Committee Members and results from FES2014[8] (Lyard *et al.* 2021), allowing calculation of astronomical tides for stations where observation data are not available.
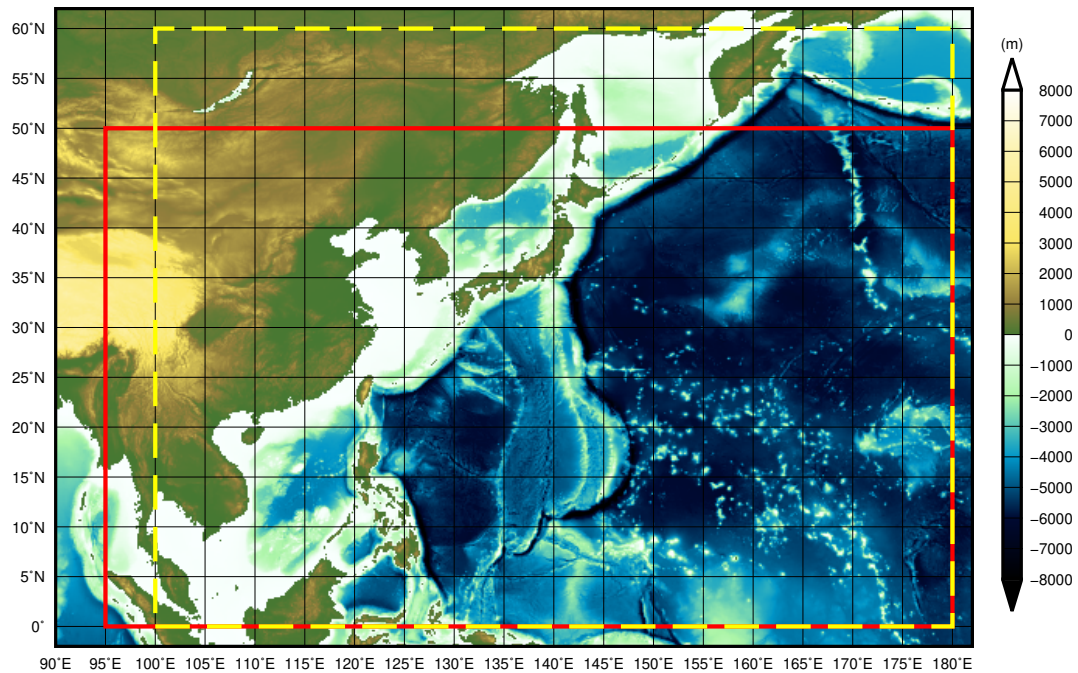

Figure 5.5.9: GEBCO 2021 topography. The red line indicates the domain of the Asia-area storm surge model, and the dashed yellow line denotes the RSMC Tokyo - Typhoon Center's area of responsibility.

5.5.2.4 Meteorological Forcing

Operation of the Asia-area storm surge model involves the blending of simple parametric TC model data and output from JMA's operational Global Spectral Model (GSM) as meteorological forcing fields. The simple parametric TC model in this resource is as per that of the Japan-area storm surge model (typhoon bogussing in Subsection 5.5.1). Related calculation requires an atmospheric model covering the Asia area, but the resolution of the GSM (13 km) is insufficient for resolving adequate TC intensity. Accordingly, meteorological forcing is generated by implanting typhoon bogussing information into atmospheric model gridded data.

5.5.2.5 Ensemble Prediction

The Asia-area storm surge model previously adopted multi-scenario predictions (Hasegawa *et al.* 2017), and six scenarios were considered. However, this was insufficient for risk management because the occurrence and intensity of storm surges strongly depend on TC tracks, and probabilistic forecast products could not be provided in this way. Against such a background, JMA introduced an ensemble prediction system with 52 members and began providing ensemble forecast products (Hasegawa *et al.* 2023) using the GSM with typhoon bogussing and the Global Ensemble Prediction System (GEPS) (Kyouda and Higaki 2015), which

---

[8]FES2014 was produced by NOVELTIS, LEGOS, CLS Space Oceanography Division and CNES. It is distributed by AVISO, with support from CNES (http://www.aviso.altimetry.fr/).

has 51 members. As the horizontal resolution of the GEPS (27 km) is considered too coarse for adequate TC prediction, typhoon bogussing is implemented for TC tracks of all GEPS members as in the GSM.

5.5.2.6 Model Specifications

Table 5.5.2 outlines the specifications of the Asia-area storm surge model. Here, an unstructured Arakawa-B approach is adopted with a grid system, and a finite volume approach is used for equation resolution with reference to the Finite Volume Community Ocean Model (FVCOM) (Chen *et al.* 2003) and the Finite-volumE Sea ice-Ocean Model (FESOM2) (Danilov *et al.* 2017). The resolution of the unstructured grid ranges from 1.5 to 50 km, becoming fine in coastal areas and coarse in open seas (Figure 5.5.10). The model covers most of the RSMC Tokyo - Typhoon Center's area of responsibility (Figure 5.5.9), running every six hours and calculating storm surge predictions up to 132 hours ahead. When no TCs are present, a single calculation is conducted with GSM prediction. If one or more TCs are present or expected in the model domain, ensemble predictions for 51 members are additionally carried out based on the GEPS with wind and pressure fields modified by typhoon bogussing.

Three-hourly distribution maps of the whole domain and enlarged versions showing only areas around the TC are available up to 132 hours ahead. The time-series charts provided include data on predicted/astronomical tides, storm surge, sea level pressure and surface wind. Time-series charts for 78 locations are currently provided to Typhoon Committee Members.

Table 5.5.2: Specifications of the Asia-area storm surge model

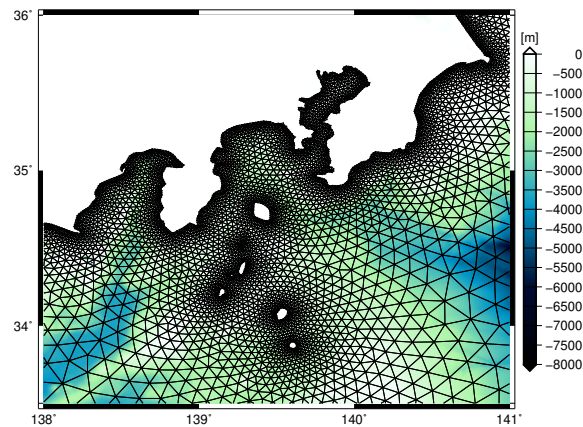| Model	two-dimensional non-linear model
Grid	unstructured Arakawa-B grid
Region	0° - 50°N, 95°E - 180°E
Resolution	1.5 - 50 km
Time step	4 seconds
Initial time	00, 06, 12, 18 (UTC)
Forecast period	132 hours
Member	TC case: 52 members (GSM + GEPS 51 members with typhoon bogussing)
	no TC case: 1 member (GSM)

Figure 5.5.10: Unstructured grid around the Kanto region in the Asia-area storm surge model. JIGSAW (Engwirda 2017) is used as a mesh-generating tool.

5.5.2.7 Verification

To evaluate the performance of the Asia-area storm surge model, accuracy was verified by comparing predicted and observed values of hourly storm surge for numerous tide stations in the Japan and Asia areas over the statistical period from June 2018 to March 2021. Figure 5.5.11 shows a scatter diagram of storm surge hindcasts against observation values for 214 tide stations in the Japan area (left) and eight tide stations in the Asia area (right). Note that the GSM resolution is 20 km in this statistical period. Most storm surge prediction errors lie within the range of ± 50 cm in both panels, although some underestimation is seen for reasons similar to those detailed in Subsection 5.5.1.5 for the Japan area. For the Asia area, underestimations were seen at Quarry Bay (Hong Kong) for the intense Typhoon Mangkhut (T1822), and the atmospheric model (GSM) did not adequately resolve sea level pressure and surface wind. Inaccuracy in topographical expression and calculation in the Asia-area storm surge model also caused underestimation.

Yearly verification details are provided in the Annual Report on the Activities of the RSMC Tokyo - Typhoon Center [9].
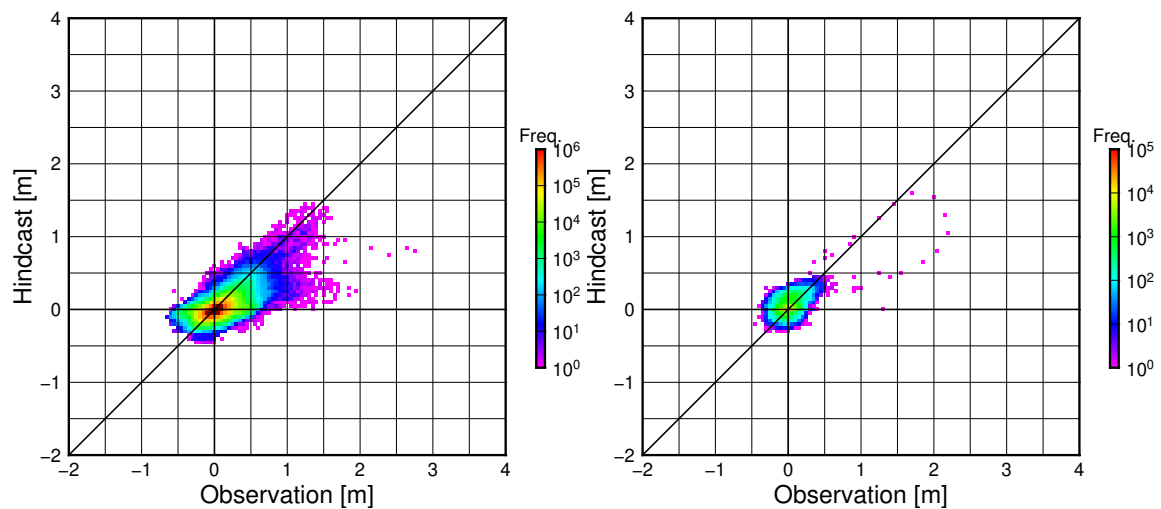

Figure 5.5.11: Scatter diagram of storm surge hindcast values against observations. Left: results for 214 tide stations in the Japan area; right: results for eight tide stations in the Asia area.

Figures 5.5.12 and 5.5.13 show distribution mapping for the probability of storm surges exceeding 1 meter in height during the forecast period and time-series charts for Quarry Bay (Hong Kong) for Typhoon Ma-on (T2209), respectively. The typhoon passed northwest over the South China Sea and generated high storm surges around Hong Kong. The results show that ensemble predictions captured the potential for high storm surges and peak storm surge/tide conditions well.

5.5.3 Astronomical Tide Analysis

5.5.3.1 Introduction

The model described in Subsection 5.5.1 calculates only storm surges, defined as anomalies from the astronomical tide level. However, prediction of storm tides (i.e., storm surge plus astronomical tides) is needed for storm surge warning issuance. In 2010, JMA changed its storm surge warning criteria to cover issuance for all coastal areas of Japan in consideration of inundation risk at all points. Appropriate issuance of warnings requires calculation to determine astronomical tides in all coastal areas.

---

[9] http://www.jma.go.jp/jma/jma-eng/jma-center/rsmc-hp-pub-eg/annualreport.html

Figure 5.5.12: Distribution for the probability of storm surges exceeding 1 meter in height during the forecast period as predicted by the Asia-area storm surge ensemble prediction system with an initial time of 00 UTC on 23 August.

Figure 5.5.13: Time-series charts of storm/astronomical tides (top), storm surge, sea level pressure and surface wind (bottom) for Quarry Bay (Hong Kong) as per the Asia-area storm surge ensemble prediction system with an initial time of 00 UTC on 23 August.
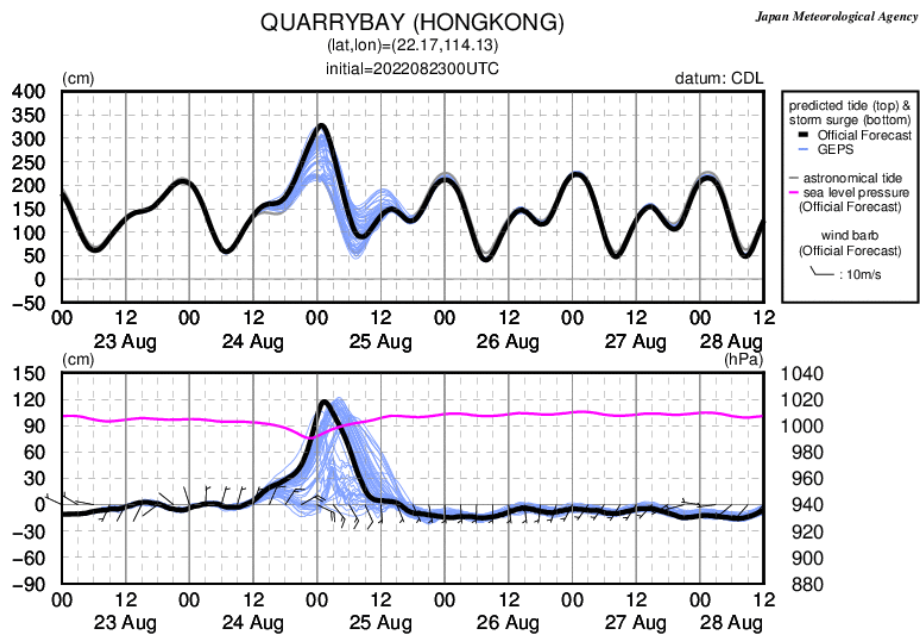
5.5.3.2 Analysis Method

Tidal variations are expressed as a composite of periodic oscillations with various frequencies, as observed with semi-diurnal, diurnal and annual tides. Semi-diurnal and diurnal tides are caused by lunar and solar gravitational forces, while annual tides are brought by seasonal variations in seawater temperature and sea surface pressure. Harmonic constants are sets of amplitudes and phases for individual tidal constituents. Harmonic constants at tide station points can be derived by analyzing hourly tidal observation data, but cannot be determined for arbitrary coastal points where such data are unavailable using this method.

To enable analysis of astronomical tides for the whole of Japan's coast, both short-period (semi-diurnal and diurnal) and long-period tides (annual) tides are considered as shown in Figure 5.5.14. The constituents used in this method (Takasa *et al.* (2011)) are shown in Table 5.5.3.
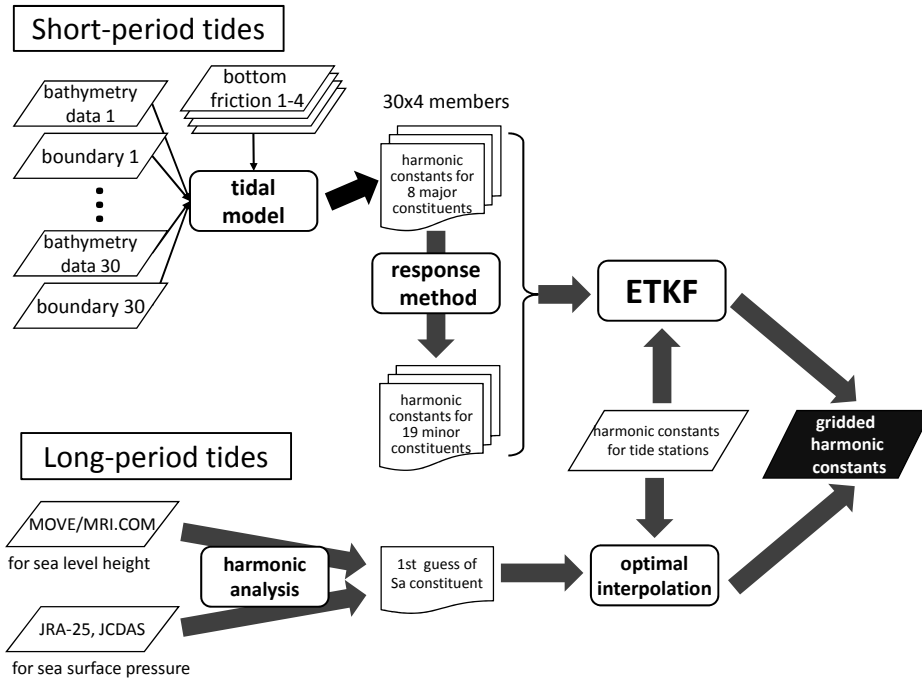
Figure 5.5.14: Flow of astronomical tide analysis

5.5.3.3 Short-period Tides

Eight major constituents with relatively large amplitudes (K1, O1, P1, Q1, K2, M2, N2 and S2; Table 5.5.3) are estimated using the Oregon State University Tidal Inversion Software (OTIS) tidal model package (Egbert and Erofeeva 2002), which involves data preparation, ocean dynamics and data assimilation. Only the linearized version of ocean dynamics (a tidal model), in which Fourier transform is applied to eliminate time variation, is used:

$$i\omega U - fV + gH\frac{\partial \zeta}{\partial x} + \kappa U = F_U \tag{5.5.12}$$

$$i\omega V + fU + gH\frac{\partial \zeta}{\partial y} + \kappa V = F_V \tag{5.5.13}$$

$$\left(\frac{\partial U}{\partial x} + \frac{\partial V}{\partial y}\right) + i\omega\zeta = 0 \tag{5.5.14}$$

Table 5.5.3: Constituents used in astronomical tide analysis.

Name	Type	Major/Minor	Name	Type	Major/Minor
S_a	annual	-	θ_1	diurnal	minor
$2Q_1$	diurnal	minor	J_1	diurnal	minor
σ_1	diurnal	minor	OO_1	diurnal	minor
Q_1	diurnal	major	$2N_2$	semi-diurnal	minor
ρ_1	diurnal	minor	μ_2	semi-diurnal	minor
O_1	diurnal	major	N_2	semi-diurnal	major
MP_1	diurnal	minor	ν_2	semi-diurnal	minor
M_1	diurnal	minor	M_2	semi-diurnal	major
χ_1	diurnal	minor	λ_2	semi-diurnal	minor
π_1	diurnal	minor	L_2	semi-diurnal	minor
P_1	diurnal	major	T_2	semi-diurnal	minor
K_1	diurnal	major	S_2	semi-diurnal	major
ψ_1	diurnal	minor	R_2	semi-diurnal	minor
ϕ_1	diurnal	minor	K_2	semi-diurnal	major

where ω is the tidal constituent frequency, U and V are the x- and y-components of current integrated from the sea surface to the bottom, respectively, f is the Coriolis parameter, g is gravity acceleration, H is depth, ζ is the anomaly from mean sea level, κ is the dissipation coefficient of bottom friction, and F is the tide-generating force.

The Ensemble Transform Kalman Filter (ETKF) (Bishop *et al.* 2001) is used to assimilate harmonic constants at tide stations. As the model results contain uncertainties due to a lack of resolution and accuracy in bathymetry data and lateral boundary conditions, perturbations are added to these conditions to create an ensemble. There are 30 sets of bathymetry data (incorporating random errors) and boundary condition data generated by blending results from four tidal models (NAO.99Jb (Matsumoto *et al.* 2000), FES2004 (Lyard *et al.* 2006), GOT00.2 (an update to Ray (1999)) and TPXO (Egbert and Erofeeva 2002)). Four sets of bottom friction data are also used in consideration of the influence of such friction on tidal amplitude (Yano *et al.* (2010) and An (1977)). The 120 ensemble members are associated with a combination of the 30 sets of bathymetry and boundary condition data and 4 sets of bottom friction data.

A total of 19 minor constituents (see Table 5.5.3) are estimated from major constituents of similar frequency using the response method (Munk and Cartwright 1966).

5.5.3.4 Long-period Tides

The first guess of annual constituents (S_a) is derived from the results of harmonic analysis of reanalyzed sea level height from MOVE-WNP (see Section 5.3 and Usui *et al.* (2006)) corrected with sea surface pressure from the Japanese 25-year Reanalysis (JRA-25) and the JMA Climate Data Assimilation System (JCDAS) (Onogi *et al.* (2007)) assuming hydrostatic balance. This is modified using harmonic constants for tide stations with the optimal interpolation method.

5.5.3.5 Verification

To verify astronomical tide analysis based on the method described, the outcomes are compared with those from harmonic constants at tide stations. Figure 5.5.15 shows a comparison of root mean square errors (RMSEs) for the respective distributions. For most stations, the error is less than 3 cm, although larger values are observed for some stations, especially in bays and inland sea areas.
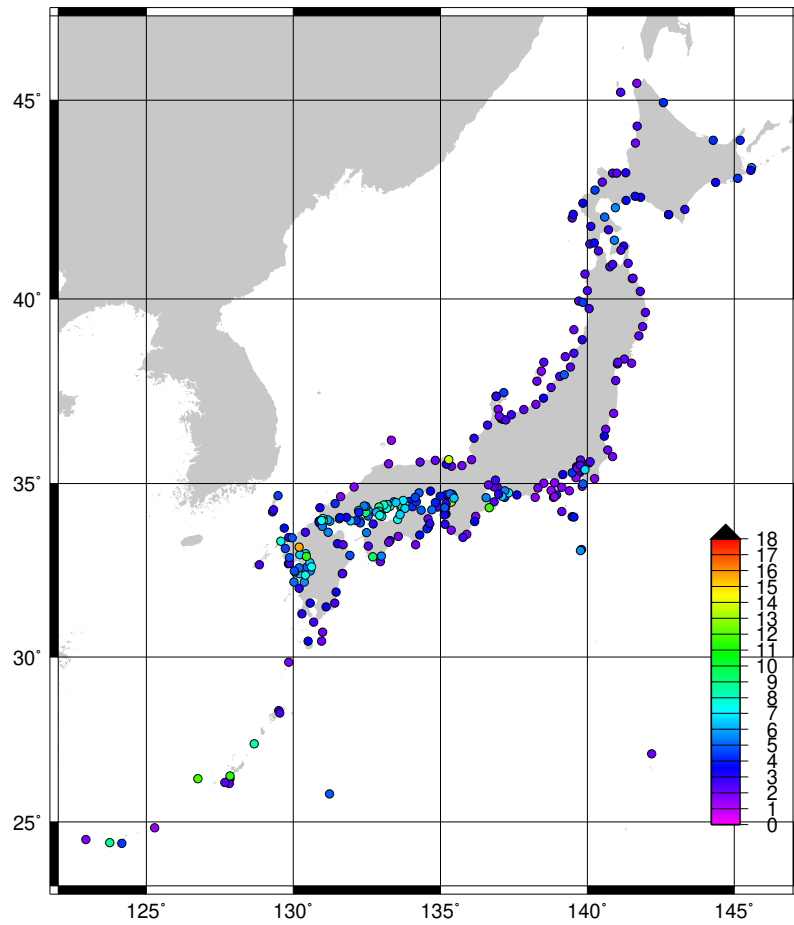
Figure 5.5.15: Distribution of RMSEs from astronomical tide analysis. The unit is cm.

5.6 Oil Spill Prediction Model

5.6.1 Introduction

In the 1990s, large-scale oil spills (such as those involving the vessels ABT Summer, MB Braer and Sea Empress) frequently occurred around the world. In Japan, the wrecking of the Russian tanker Nakhodka resulted in a serious oil spill in the Sea of Japan in January 1997, causing major environmental damage along Japan's western coast. Following the Japanese Government's subsequent consideration of countermeasures for large-scale oil spills, JMA has operated its Oil Spill Prediction Model since October 1999.

The model predicts the large-scale behavior of oil spilled in offshore seas. Based on accident information from the Japan Coast Guard, JMA operates the model to produce forecasts with lead time up to 240 hours. The results are provided to personnel responsible for emergency response operations.

The model is applicable to the entire western North Pacific. The domain of calculation is selected from seven settings from $0.8° \times 0.8°$ to $12° \times 12°$ in latitude and longitude based on consideration of incident conditions.

5.6.2 Basic Equation

The oil spill prediction model is generally described by the following equation including terms of advection and diffusion,

$$\frac{dC}{dt} = \frac{\partial C}{\partial t} + \mathbf{V} \cdot \nabla C = \nabla \cdot (K \nabla C) + S \tag{5.6.1}$$

where C is pollutant concentration, t is time, $\mathbf{V}$ is advection velocity, K is the turbulent diffusion coefficient, and S (referred to as the source term) represents the process involved in changing the total amount of oil spilled through changes in oil properties.

Equation (5.6.1) in general can be numerically solved either by calculating C directly using the finite difference method or by simulating the behaviors of a large number of particles representing oil components. The latter approach is used in JMA's Oil Spill Prediction Model. Spilled oil is expressed as numerous particles $C_n (n = 1, 2, \cdots)$ using:

$$C_n \{\mathbf{x}(t + \delta t), s(t + \delta t); t + \delta t\} = \Phi[C_n (\mathbf{x}(t), s(t); t), \delta t] \tag{5.6.2}$$

where $\mathbf{x} = (x, y, z)$ indicates the position of each particle and s is the chemical status of the oil. Φ is a general function describing oil property changes over time.

In the advection term, the effects of surface winds, ocean waves, and ocean currents are taken into account as potentially major factors. Ekman drift current generated by sea surface winds is an example of such as an influence. In the JMA model, surface flows are determined as 2.5% of the wind speed with an angle of $15°$ clockwise with respect to the wind direction. As another example, Stokes drift involves forward movement of particles at the sea surface in the wave direction as a result of wave motion back and forth in each wave cycle. This effect is more significant when high waves are present, and is independent of wind when swell is predominant. Accordingly, Stokes drift is included explicitly and calculated from predictions by JMA ocean wave models. Ocean currents are provided by the JMA Ocean Data Assimilation and Prediction System for the seas around Japan (MOVE-JPN; Subsection 5.3.3).

The three-dimensional diffusion of oil is basically calculated via the shear diffusion treatment proposed by Elliott (1986). Surface flow is assumed to have a logarithmic profile in the vertical direction, and spilled oil is assumed to be carried at a particular horizontal speed in each water level. The shear mechanism is also associated with vertical diffusion. Spilled oil is divided into a large number of droplets with varying levels of buoyancy in line with their size. Consideration of this buoyancy and the present depth of oil drops allows determination of oil motion in the vertical direction and clarification of whether the oil floats on the surface.

In addition to the above shear diffusion process, isotropic diffusion may also be generated by small scale eddies and similar influences as estimated using the constant diffusion coefficient $K_h = 95.0 \text{ m}^2/\text{s}$. As such diffusion may be greater in conditions of strong wind or high waves, the influence is parameterized with additional diffusion coefficients:

Table 5.6.1: Oil Spill Prediction Model specifications

Applicable area		15°S – 63°N, 99°E – 80°W
Domain of calculation		7 options ($0.8° \times 0.8° - 12° \times 12°$)
Grid spacing		7 options (2–30km), according to the domain of calculation
Number of grids		41×41
Prediction period		240 hours
Physical and chemical process	Advection	Ekman drift (estimated from wind field of Global Spectrum Model) Stokes drift (estimated from wave field of Global/Coastal Wave Models) Ocean current (MOVE-JPN)
	Diffusion	Elliott (1986) etc.
	Evaporation	Fingas (2010)
	Emulsification	Reed (1989)

$$\begin{cases} \text{waves: } K_{wv} &= 500.0 H_w^2 / T_w \\ \text{winds: } K_{wnd} &= 5.0 W^3 / g \end{cases} \tag{5.6.3}$$

where H_w and T_w are the wave height and period, W is wind speed, and g is gravitational acceleration. The coefficients are empirically determined on the basis of actual cases.

Additional diffusion of oil parcels is estimated from the total value of the diffusion coefficients (K_h, K_{wv}, and K_{wnd}). Specific values are calculated using the random walk method with such diffusion assumed to be horizontal.

Due to the complex behavior of spilled oil, consideration of all related chemical processes is largely impractical. Accordingly, only evaporation and emulsification are considered as major processes. Evaporation is estimated using empirical formulae (Fingas 2010), in which the evaporation rate E_v (%) of most oils can be expressed by the form of either the logarithmic or the root profile over time.

$$E_v = \begin{cases} (a + b \cdot T) \ln t \\ (a + b \cdot T) \sqrt{t} \end{cases} \tag{5.6.4}$$

The constant coefficients a and b are based on experimental results and are listed in the Environment Canada oil data catalogue. T represents oil temperature, and is assumed to be equivalent to sea surface temperature (SST). t is the number of minutes elapsed since the spill.

Emulsification is calculated using the formula of Reed (1989), by which the water content F_{wc} is estimated as:

$$\frac{dF_{wc}}{dt} = 2.0 \times 10^{-6} (W + 1)^2 \cdot \left(1 - \frac{F_{wc}}{C_3}\right) \tag{5.6.5}$$

where W (m/s) is wind speed. C_3 is a constant parameter for the upper limit of water content, and differs among oil types. Oil density is also calculated in consideration of water content, which can change the behavior of oil.

The specifications of the Oil Spill Prediction Model and related processes are summarized in Table 5.6.1.

5.6.3 Products

The model is operated in the event of a large-scale oil spill in offshore deep-water seas, where short-term tidal currents can be negligible. The results of oil spill prediction are provided to the Japanese Government and/or the Japan Coast Guard along with various marine meteorological charts. An example of prediction is shown in Figure 5.6.1.

(a)Forecast period: 24 h   (b)Forecast period: 48 h   (c)Forecast period: 72 h

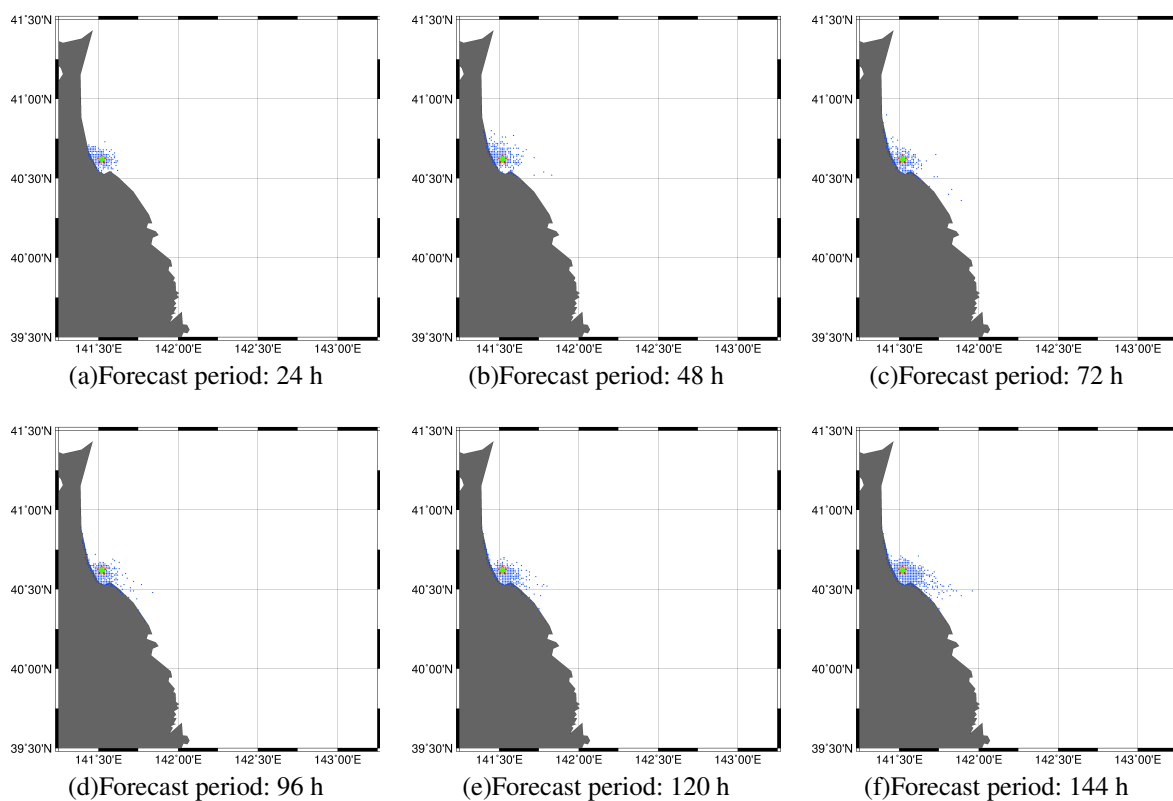(d)Forecast period: 96 h   (e)Forecast period: 120 h   (f)Forecast period: 144 h

Figure 5.6.1: A simulation for the sea east of Japan supposing an accident at 19UTC on 11 Aug 2021 at 40.37 °N 141.31 °E. The stars show the accident location, and the rhombuses show the source of the spillage (assuming the source is carried by ocean currents). The area and amount of spilled oil are indicated by dot distribution.